Unified modeling and feasibility study of novel green pathway of biomass to methanol/dimethylether

Zohreh Ravaghi-Ardebili, Flavio Manenti *

Politecnico di Milano, Dipartimento di Chimica, Materiali e Ingegneria Chimica "Giulio Natta", Piazza Leonardo da Vinci 32, Milano 20133, Italy

Received 3 January 2014
Received in revised form 3 February 2015
Accepted 8 February 2015

1. Introduction

Process integration is generally defined as being related to the process design to emphasize the unity of the process and interaction between different unit operations, or different plants in operation, in order to employ the resources effectively and

* Corresponding author. Tel.: +39 02 2399 3273; fax: +39 02 7063 3280.
E-mail address: flavio.manenti@polimi.it (F. Manenti).

minimizing the costs and energy consumption throughout the process [1–3]. Considering the environmental concerns to meet the free emission approaches is another significant motivation of the process integration, which is accomplished not only designing new facilities and process layouts, but also replacing some tradi-tional resources by new and greener one [4–7]. From this perspec-tive, it would be synergistic to provide the combination of the various energy sources, renewable and non-renewable sources, and process engineering is unavoidably the key-step in combining and integrating sources in a sustainable way with an additional advantages for the energy sector and industries [6]. The generation of clean and emission free source of power for facilities plays a key role in the sustainability of the processes and, as it is understandable, the dependency of the chemical industries on the steam availability falls into this element [8,9]. It is therefore promising to provide an alternative for the clean production of steam rather than traditional and common technologies, which are complex, highly sophisticated and expensive processes [9]. Traditionally, power plants are based on coal-fired power/steam generation. All conventional sources of steam generation such as gas turbine combined cycle (CC) [10,11], integrated gasification combined cycle (IGCC) [12–14], and pressurized fluidized bed combustion (PFBC) [15,16] are fuel based steam generation processes [8]. Environmentally speaking, decreasing the carbon footprint in chemical plants requires the intensive attempts to optimize the energy requirements by reduction of the consumption of the energy and lessen the carbon emissions associated with the remaining energy. The idea of shifting the energy resources of chemical plants to renewables such as solar and wind is reinforced if appropriate storage technologies are developed [6] to make continuous the power supply that comes from a discontinuous source. The concentrating solar power (CSP) plant is suggestively an attractive opportunity for power generation considering it as the source of energy without carbon footprint, and performing in a form of electricity or steam. It might be claimed that the CSP plant is a unique renewable resource of power generation, which can easily be coupled with other units to operate only by the means of thermal energy storage (TES) to make it highly dispatchable throughout the process [17,18]. However, it becomes more complex for research investigation relying on modeling and simulation tools due to the lack of reliable models and appropriate accessible simulators to model the renewables and demonstrate the feasibility of such facilities. The complexity is found especially when the simulation is required for the entire plant, which includes the integration of non-conventional units, complex and non-ideal thermodynamic data and libraries, innovative equipment and uncommon components for the process operations. Many of the above elements are not included in the commercial packages for process modeling, typically addressed to the oil and gas and process industry [19], and have to be developed ex novo and integrated and synchronized in these packages. Although, few dynamic modeling and simulations were performed to improve the knowledge and the effectiveness of solar plants facing design [20], numerical simulation [21], economic issues [22] monitoring [23], prediction [24] and control [25] of the ther-mal energy storage methods, they are still not based on well-established commercial dynamic simulators. In investigating the reason, it is evident that these types of plants contain operating units (i.e., the solar collector) deeply dissimilar to the conventional units adopted elsewhere [26] and traditionally included in the model library for process simulations such as AspenHysys and Pro/II. Therefore, it would be possible to either provide a new model or transforming the existing models to search for a reasonable accuracy for the simulation. Some issues for the CSP plant simulation have been already faced by the authors in prior works [18,27], mainly dealing with the heat exchange train for steam generation from hot molten salt streams.

Unavailability of mathematical models is one of the main issue making stiff the studies of novel process layouts that want to integrate renewable sources in the flowsheeting procedure and economical process assessments as well as slowing the advances in process engineering [18,19].

About the gasification process, it is obvious that although the reserves of coal are abundant and widespread geographically over the world [28,29], due to the price in comparison with oil [30–32] and also, the environmental issues competitive with biomass, it is not well allocated in the emission free and inexpensive category of feedstock for the energy sector [33,34]. Relying on addressed reasons, the focus on biomass was and is concentrating severely rather than coal and activities are driven toward bio-products, che-mical commodities and bio-fuels in the near future starting from second, but also third, generation biomass. The Horizon 2020 pro-gram of the European Community is a clear example of this energy roadmap. Furthermore, biomass promises to provide the sustainability as a renewable feedstock. Following these approaches, replacing fuel-based power plants with renewable and clean sources of energy could bring benefits in comparison with the traditional ways of steam generation processes. Although several works have been accomplished in the gasification modeling and kinetics development [35,36], design of the gasifier [37,38] and effective operating conditions [39–42], no significant work is found on low-temperature biomass gasification in the literatures, which is the typical condition of the solar-powered steam generation taken into consideration in this work. The practical feasibility of the proposed low-temperature biomass gasification process is therefore investigated. The gasification unit has the ability to become an important and key facility in the energy and chemical process industry [43]. Coupled with this, nowadays, methanol is advocated to substitute oil and dimethylether (DME) as substitute natural gas [44], both of which are predominantly produced by steam reforming of methane (natural gas) and subsequent synthesis reactions of the produced syngas to methanol and, then, to DME. However, any source of organic material could be converted into syngas and so, methanol. Therefore, biomass from organic urban/industrial/agricultural waste as feedstock could become a source of methanol in the near future [43,45–49].

Since the introduction of the high-pressure methanol synthesis in the 1920s, several technologies have been introduced to achieve low-pressure synthesis [50]. Nowadays, Lurgi, Haldor Topsøe and Davy Process Technologies allows to produce methanol at 60–100 bar from syngas (CO and H_2 mixture), which is usually obtained by means of steam reforming operations [44]. The metha-nol synthesis reactor is usually based on two fixed-bed tubular sections [51–54], a gas-cooled and a water-cooled section, although several other configurations have been proposed [43,55,56]. This paper is aimed at discussing the methanol/DME synthesis fed by the syngas produced in the biomass gasification process. The so-called one-step technology for the co-current production of methanol and DME is considered. It must be evoked that H_2:CO ratio for methanol synthesis could be adjusted either in situ, where the reverse water gas shift reaction is active on the catalyst or using an ad hoc water gas shift reactor.

An overview of the unified plant of biomass-to-methanol/DME together with the tools adopted for the study is given in Section 2; CSP plant and TES are described and modeled in Section 3; biomass gasification process is characterized, designed, and simulated in Section 4; the one-step technology for methanol/DME production is deepened in Section 5.

2. Overview of the unified plant and tools adopted

The main issues in modeling and studying the practical feasibility of a novel solar-driven route from biomass to MeOH/DME

are related to the need of different tools and interdisciplinary competences. Indeed, the discontinuous nature of CSP and the intrinsic dynamic behavior of TES technologies unavoidably lead the attention to the development of dynamic simulations. Conversely, steady state models for biomass gasification and MeOH/DME synthesis are enough to characterize such systems. Nevertheless, in these latter cases, there is the further complexity of considering either multi-phase, multi-scale and multi-component models (gasification process) easily leading to large-scale nonlinear systems or to handle networks of tubular reactors subject to very tight operating conditions (methanol synthesis process).

Specifically, available commercial packages have been selected in which, the simulation can be carried out with existing models already implemented in these suites, whereas dedicated models have been developed when high reliability is required for the model prediction as local viewpoint as well as for the overall feasibility study. A general overview of the flowsheet is given in Fig. 1.

PRO/II steady-state simulator released by Simulation Science [57] is the selected package to model all the units downstream the biomass gasifier up to the methanol synthesis reactors. The simulation suite DYNSIM by Simulation Science [58] is selected to characterize the intrinsic dynamic nature of the CSP plants. The selection of DYNSIM suite is also related to the need for the best compatibility among all the accessible simulation tools and to the flexibility of this simulator in exchanging data in real-time with the other packages and models to ensure the complete data synchronization during the calculations. The biomass gasifier and MeOH/DME synthesis reactors are modeled and simulated using MS Visual C++ and the BzzMath library [59,60], which provide the possibility to exploit object-oriented programming and parallel computations [61]. In addition, MS Visual C++ is adopted to improve the model of the economizer unit for heat exchange of the CSP plant, since it is a critical node where the molten salts of the CSP could start crystallization and solidification and, hence, deep accuracy is needed for the unit. Such an advanced model has been fully integrated in the DYNSIM environment [62] and it can be considered as a dynamic extension of HTRI standards for heat exchange calculations [63]. In this embedded context, MS Excel supports the entire models and simulations as IT bridge to gather the information and data derived from each different envi-ronment and manage them to encompass them together.

3. Concentrating solar power plant: steam generation

CSP plants are characterized by a solar field to collect solar radiation, a heating transfer fluid (HTF) to trap the solar energy and move it elsewhere in the plant and a train for heat exchange and, often, electric energy generation via steam production. Beyond these sections, an energy storage system is necessary whenever the solar energy has to be transformed into continuous supply of energy or steam. There are different techniques of energy storages for CSP [64]; one of the most simple is the direct thermal energy storage (TES), which consists of at least one tank for physi-cal storage of HTF. In case of one tank only is adopted, the liquid is heated and cooled in the same unit according to day and night operations of the CSP. It is called the thermocline system. When the tanks for thermal energy storage are two, they are progressive-ly loaded and unloaded by HTF, the one with the hot HTF is filled daytime, the other with the cold HTF is filled during the night [65–67] (Fig. 2).

The designed process (Fig. 2) depicts the series of linear-parabolic solar troughs (Solar-101), which aim at heating the HTF driven in by harvesting the solar energy through the day. The vessels (V-201), (V-202), and (V-203) are pointing to molten salt storage tanks, which store molten salt as the initial supplier of molten salt into the plant, cold storage and hot storage, respectively. The supplier tank (V-201) operates as the supporter of molten salt into the plant in which molten salt is positioned on the start-up lines (S-101, S-102, and S-103) and supplied into the cold tank at the CSP plant startup. These lines are useful for plant startup and HTF maintenance/exchange only and they are normally no-flow during the conventional operations since no make-up of molten salts is necessary. Once the adequate amount of molten salt meets the demand plant (cold tank), it starts to drive away from V-202 to V-203 passing through Solar-101, and imposing the nominal solar radiation for typical sunny days into the system (set in solar line, i.e., S-104 and S-105). It is worth mentioning that this line is disabled at night or whenever the solar radiation cannot be harvested (according to meteorological conditions).

The heat exchanger (HEX) train consists of four units that encounter in series the HTF coming from the energy storage: the second steam superheater (E-111), the first steam superheater (E-112), the boiler (E-113), and the economizer (E-114). Also a vessel boiler (E-115) is included. The HEX block generates the steam (generation line starting from S-107 to S-120). The molten salt with a flowrate of 135 kg/s passes through the heat exchanger train, with the ideal assumption of maximum performance on the exchange surface (3831 m^2). The overall heat transfer coeffi-cient is 0.58 $kW/m^2/K$. To describe the heat transfer procedure, fol-lowing the streams starting from V-203 toward HEX block, the process utilizes E-111, E-112, E-113, and E-114 to heat exchange and the boiler (E-115) to generate the steam. The steam is sent to the turbine (T-311), cooled down passing over the condenser (E-116) and the cooling tower (E-117). The cooled water in the next step is recycled back to the steam/water loop (S-119). The temperature of the molten salt progressively decreases from 550 °C to 290 °C providing heat and converting the water into steam.

As the HEX block is a crucial section for the effectiveness of the CSP plant and the process control systems to manage and monitor the temperature of molten salts, the key parameters for the overall plant are associated to the economizer unit. Basically, the outlet temperature of the molten salt in the economizer cannot be smaller than a safety threshold to prevent possible crystallization and, at the same time, it cannot be too high to prevent possible degradation of the HTF itself. Thus, the fresh water fed to the water/steam cycle, and specifically, to the economizer should be slightly manipulated to safeguard these objectives. Although, the other units (e.g., power block and solar collector field) of CSP plants [68–70] were earlier investigated in the literature, no specific mod-el was found for the economizer unit as the critical unit of this section [71–73] (Figs. 3 and 4).

3.1. Dynamic modeling of economizer (E-114)

The economizer is a critical unit due to the lowest temperature achieved by molten salts along the process (290 °C), slightly larger than the freezing point (270 °C). Practically, the temperature of the molten salt flowing out of the process side of the economizer is measured regularly, monitored and controlled to prevent any crystallization of the HTF and, consequently, any undesired malfunction/shutdown of the CSP process. Due to its importance, a dedicated model for economizer has been implemented in MS Visual C++ and added to the dynamic simulation carried out using DYNSIM. Furthermore, due to the missing thermodynamic data of molten salts (60% $NaNO_3$ and 40% KNO_3), a dedicated library of components and thermodynamic for solar units have been developed and implemented into DYNSIM.

The following assumptions have been used to develop the first-principles model for the economizer:

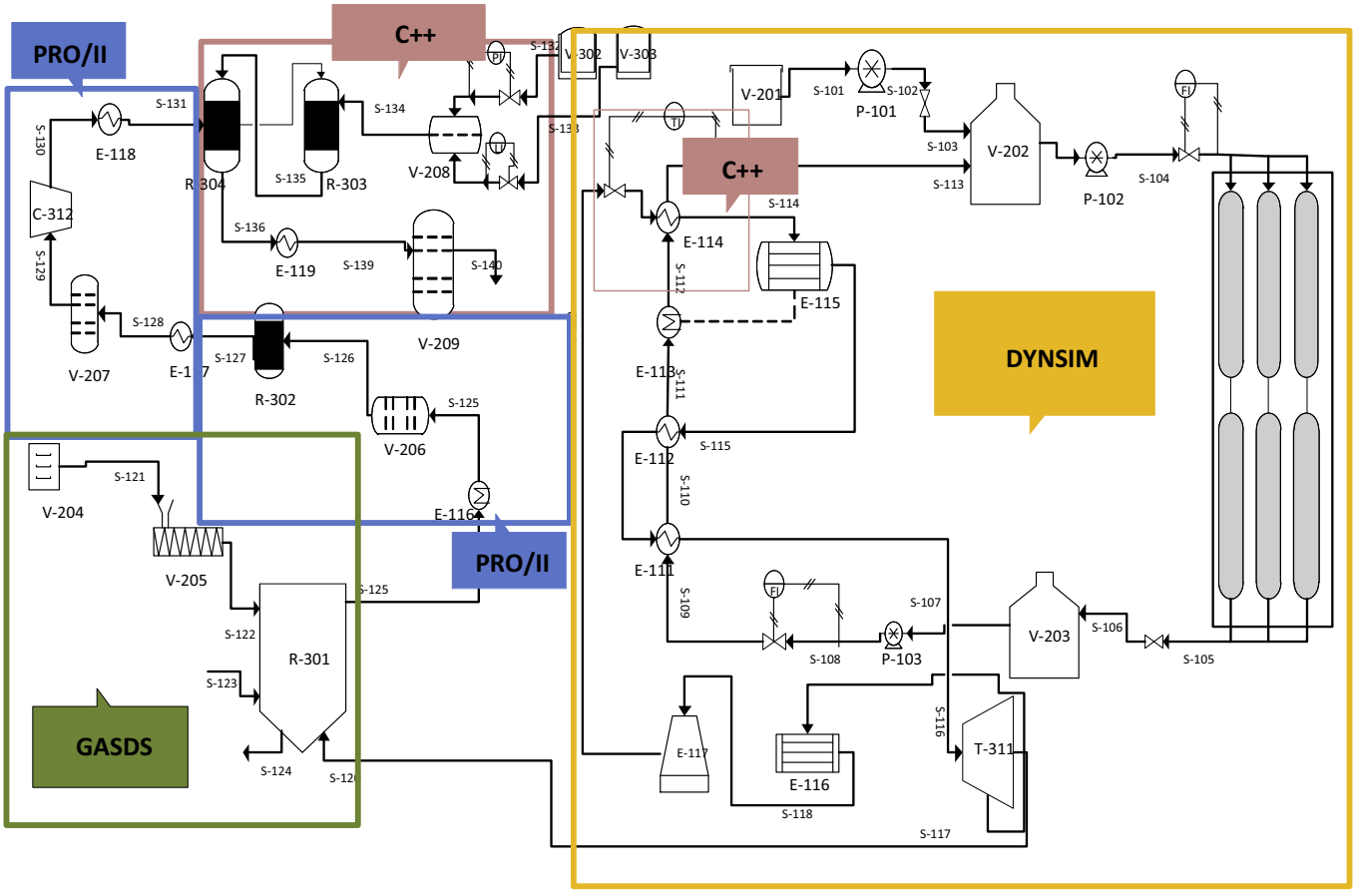

Fig. 1. Biomass-to-methanol/DME synthesis process layout.

- negligible radial gradients in the tube bundle and in the single tube as well;
- cold fluid (water) in the shell side;
- heat transferred from molten salt (T) to the metal wall (T_M) and, next, to the water;
- negligible potential and kinetic energy;
- simplified forms for internal energy and enthalpy;
- negligible diffusive flow with respect to the bulk flow.

Apart from the distributed nature of the heat exchanger, the energy balance depends on the inlet and outlet convection terms and heat losses to the ambient:

$$\frac{dH}{dT} = H_{in} - H_{out} + Q_s$$

$$\frac{d(m \cdot \dot{h})}{dt} = m \cdot \dot{h}_{in} - m \cdot \dot{h}_{out} + Q_S$$

$$\frac{d(m \cdot Cp \cdot T)}{dt} = m \cdot Cp_{in} \cdot (T_{in} - T_{ref}) - m \cdot Cp_{out} \cdot (T_{out} - T_{ref}) + Q_s$$

Since mass and specific heat can be considered constant and assuming the system as perfectly mixed, the following general form is derived:

$$m \cdot Cp \cdot \frac{dT}{dt} = m \cdot Cp_{out} \cdot (T_{in} - T_{out}) + Q_s$$

In contrast, a more detailed model must be used to match the relevant task of the economizer, which is the assurance of the exit temperature of molten salt at 290 °C. Thus, the incremental mathematical model for thermo-hydraulic calculations of the shell and tube exchangers is selected according to HTRI (Xist) standard and extended from the steady-state to the dynamic case [63]. It means that the unit is discretized in a certain number of volumes and specific a relationship (based on flow heat exchange conditions) is applied for each element. At the latest and best knowledge of the authors, the proposed HTRI standard-based dynamic model is implemented for this unit for the first time:

- The economizer is modeled with 9 baffles and split into 10 elements along the longitudinal axis. Each element corresponds to the volume between two diaphragms or between a diaphragm and the tube plate (the first and the last element).
- Each element is split one-by-one into 6 windows; two external and internal windows, and also, two cross zones. It is promising to exploit the longitudinal symmetry of the unit in order to reduce the number of variables of dynamic model.
- There is no vertical variation of temperature. Therefore, discretization is not necessary for the vertical axis.

By considering the adopted discretization of inlet and outlet elements, the ultimate number of volumes is 30.

In addition, it is useful to consider the shell side as a continuous crossflow with respect to the tube side. Principally, the heat exchange coefficients are almost identical to those obtained in crossflow as demonstrated in other studies [72] considering the diaphragm diameter of the window is about 25% of the diameter of the shell. The physical properties are assumed as following:

- Fluid velocity is constant in each element and window.
- Pressure drops and heat losses to the ambient are negligible.

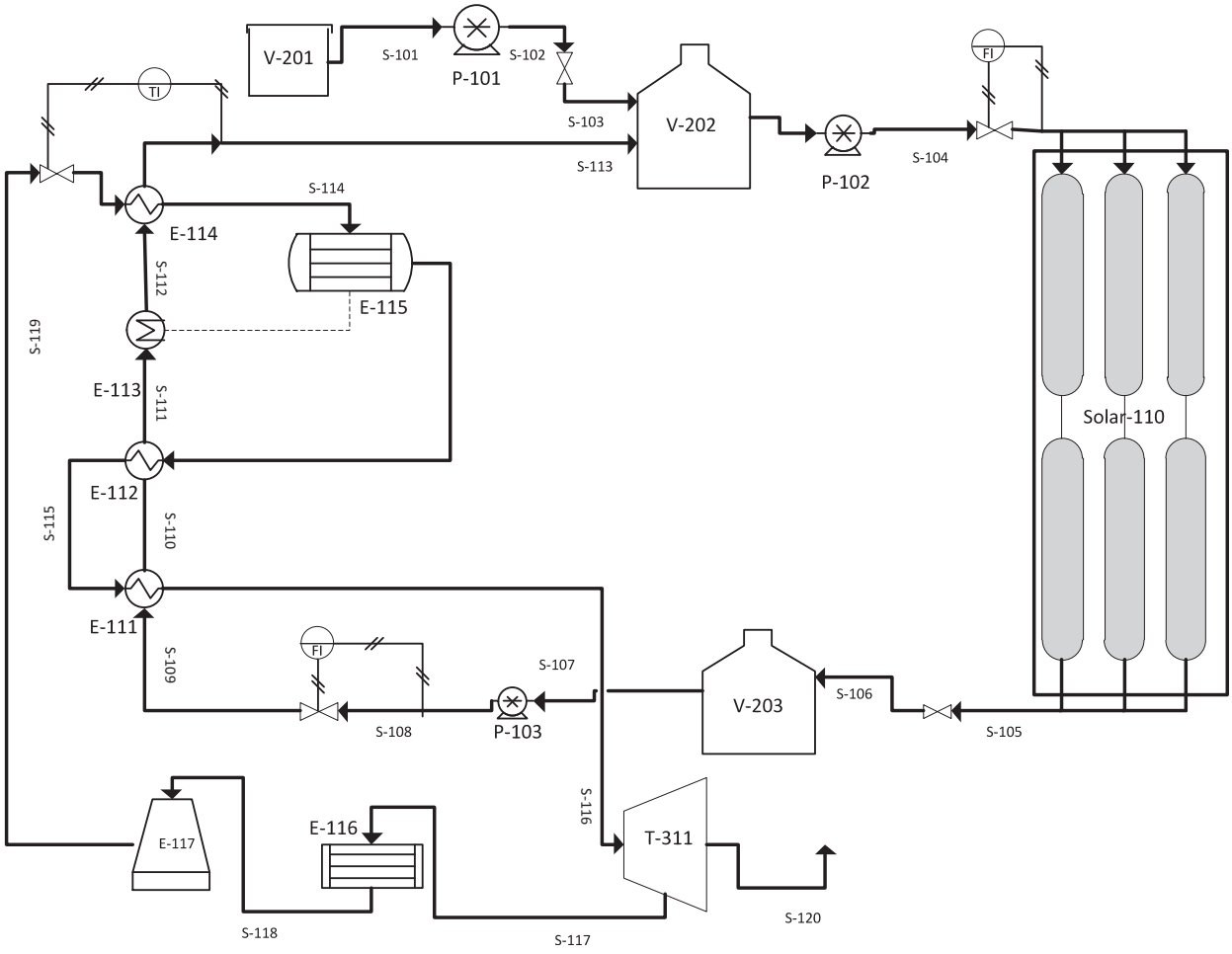

Fig. 2. Flowsheet of two-tank storage CSP plant: power generation.

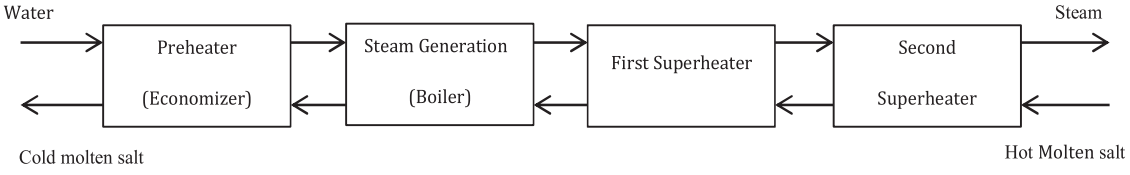

Fig. 3. Diagram of heat exchanger (HEX) train in CSP plant.

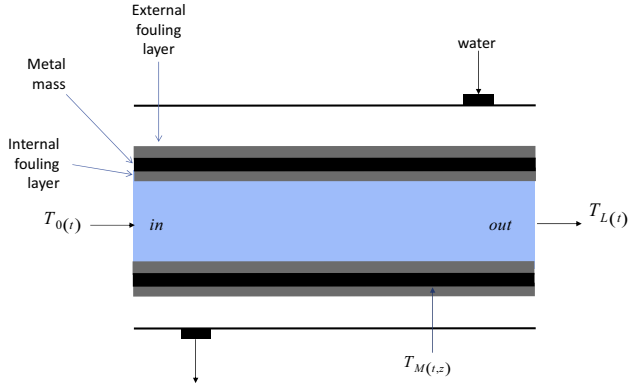

Fig. 4. Qualitative structure of economizer model.

- Temperature through the window is constant, whereas it varies from one to another and also, from each element to another one.
- The fouling of internal and external layers is negligible with respect to the dimensions of tube; no radial gradients are considered.

Considering the above-mentioned assumptions, the energy balance is stated:

$$\rho_w \cdot Cp_w \cdot V_s \frac{dT_{s,i}}{dt} = m_w \cdot Cp_w \cdot (T_{s,i-1} - T_{s,i}) + h_s \cdot A_s \cdot (T_{w,si} - T_{s,i}) - h_s \cdot A_{shell} \cdot (T_{s,i} - T_{shell,i})$$

In addition, the energy balance of the metal is defined considering the external fouling layer as the following:

$$m_{foul,shell} \cdot Cp_{foul,shell} \cdot \frac{dT_{w,s,i}}{dt} = \frac{1}{R_s} \cdot A_s \cdot (T_{w,i} - T_{w,s,i}) - h_s \cdot A_s \cdot (T_{w,s,i} - T_{s,i})$$

$$m_{metal} \cdot Cp_{metal} \cdot \frac{dT_{w,i}}{dt} = \frac{1}{R_t} \cdot A_t \cdot (T_{w,t,i} - T_{w,i}) - \frac{1}{R_s} \cdot A_s \cdot (T_{w,i} - T_{w,s,i})$$

$$m_{foul,tube} \cdot Cp_{foul,tube} \cdot \frac{dT_{w,t,i}}{dt} = h_t \cdot A_t \cdot (T_{t,i} - T_{w,t,i}) - \frac{1}{R_t} \cdot A_t \cdot (T_{w,t,i} - T_{w,i})$$

Moreover, the energy balance of the molten salts tube side and of the metal for the shell is modeled respectively:

$$\rho_{salt} \cdot Cp_{salt} \cdot V_{tube} \frac{dT_{t,i}}{dt} = m_{salt} \cdot Cp_{salt} \cdot (T_{t,k(i)-1} - T_{t,i}) - h_t \cdot A_t \cdot (T_{t,i} - T_{w,t,i})$$

$$m_{shell} \cdot Cp_{shell} \cdot \frac{dT_{shell,i}}{dt} = h_s \cdot A_{shell} \cdot (T_{s,i} - T_{shell,i}) - U_{ext} \cdot A_s \cdot (T_{s,i} - T_{ext})$$

U_{ext} is the overall heat exchange coefficient between the economizer and ambient is defined as:

$$U_{ext} = \left(\frac{1}{h_s} - \frac{OD_s}{D_{coib}} \cdot \frac{s_{coib}}{h_{coib}} + \frac{OD_s}{D_{shell}} \cdot \frac{s_{shell}}{k_{shell}} \right)^{-1}$$

The Nusselt number for external conditions (natural convection) and Grashof number [64] are calculated as follows:

$$\mathrm{Nu}_{air} = \left(0.6 + 0.387 \cdot \frac{(\mathrm{Gr} \cdot \mathrm{Pr}_{air})^{\frac{1}{6}}}{\left(1 + \left(\frac{0.559}{\mathrm{Pr}_{air}}\right)^{\frac{9}{16}}\right)^{\frac{8}{27}}} \right)^2$$

$$\mathrm{Gr} = \frac{D_S^3 \cdot \rho^2 \cdot g \cdot \beta \cdot (T - T_{air})}{\mu^2}$$

Such a detailed model for the economizer allows us to reliably predict the temperature of the molten salt.

3.2. Dynamic modeling of thermal energy storage (TES) system (V-202, V-203)

As it was mentioned above, the storing scenario of energy in CSP plants depends on the contents of the molten salt stored in the hot tank. Thus, the energy stored is entirely a capacitive system and the liquid level directly corresponds to the available thermal energy storage, which is governed by the total mass conservation principle:

$$Energy\ storage = Input - output + production$$

Since there are no reactions occurring in the energy storage tanks, for the selected energy storage the conservation principle reduces to:

$$Energy\ storage = Input - output$$

$$\frac{dM}{dt} = \dot{M}_{in} - \dot{M}_{out}$$

As the temperature inside the storage tank varies negligibly and assuming a constant density for molten salt at given ranges of temperature, then:

$$\rho_{storage} \frac{dV_{storage}}{dt} = \rho_{in} \dot{F}_{in} - \rho_{out} \dot{F}_{out}$$

$$\rho_{storage} = \rho_{in} - \rho_{out}$$

where V and $\dot{F}$ are the volume of tank and the volumetric flow, respectively. Since the storage tanks are in a cylindrical shape, the horizontal section of tank (A) is constant:

$$A_{storage} \frac{dh_{storage}}{dt} = \dot{F}_{in} - \dot{F}_{out}$$

where h is the level of molten salt in storage tank. Therefore:

$$A_{hot\ tank} \frac{dh_{hot\ tank}}{dt} = (F_{in} - \dot{F}_{out})_{hot\ tank}$$

$$A_{cold\ tank} \frac{dh_{cold\ tank}}{dt} = (F_{in} - \dot{F}_{out})_{cold\ tank}$$

The linear trend of the molten salt level in both hot and cold tanks is shown in Fig. 5 and confirms the fully capacitive nature of the selected energy storage. The holdup (liquid) of hot molten salt (in other words, the thermal energy stored) gradually increases during the day, whereas the holdup of cold molten salt practically decreases. It conceptually demonstrates that while the solar radiation is harvested, some quantity of molten salt is directly consumed to generate steam, whereas some portion of that is collected as thermal energy in the hot tank. Correspondingly, the holdup of hot storage is consumed during the night since the plant needs to be supplied constantly and generates the steam, although the solar radiation is unavailable in this interval and therefore, the solar line (streams: S-104 and S-105) is not operating.

Assuming molten salt as an incompressible fluid:

$$\dot{F}_{out,hot\ tank} = \dot{F}_{in,cold\ tank}$$

$$\dot{F}_{out,cold\ tank} = \dot{F}_{in,hot\ tank}$$

The volume of storage varies linearly according to the inflow and outflow, specifically, the level of molten salt in the cold tank increases during the night and conversely, rises for the hot tank throughout the day.

Therefore, for night time:

$$\dot{F}_{in,cold\ tank} > 0$$

$$\dot{F}_{out,cold\ tank} = 0$$

In contrast, the volume of molten salt in the hot tank rises in daytime by:

$$\dot{F}_{in,hot\ tank} > \dot{F}_{out,hot\ tank} > 0$$

As shown in Fig. 5b, HTF (molten salt) is not depleted completely at night. A safety threshold is also present for liquid holdup, although theoretical study could neglect it [25].

3.3. Steam generation

The detailed simulation of the entire plant is carried out and the numerical results for the temperature trends of molten salts and water/steam loop are given in Fig. 6. As it is clear, in spite of the complexity of the dynamic nature of the process, the simulated process provided the acceptable stability for power generation (S-116 as the last steam stream exiting from HEX block, see Fig. 2). This stream resulted as being the vital one, where we can further support the unit (T-311) and reinforce the objective of this plant being a green and clean form of power generation (though low temperature steam) and support the next plant, i.e., gasifica-tion process.

The only instability observed in trends is in correspondence with the sunrise time. In this case, the adopted control scheme is able to manage the water supply in order to preserve the desired temperatures with a relatively small oscillation in the order of 10 °C. Therefore, the dynamic nature of solar energy has been converted in a constant and steady-state steam supply for the biomass gasification process.

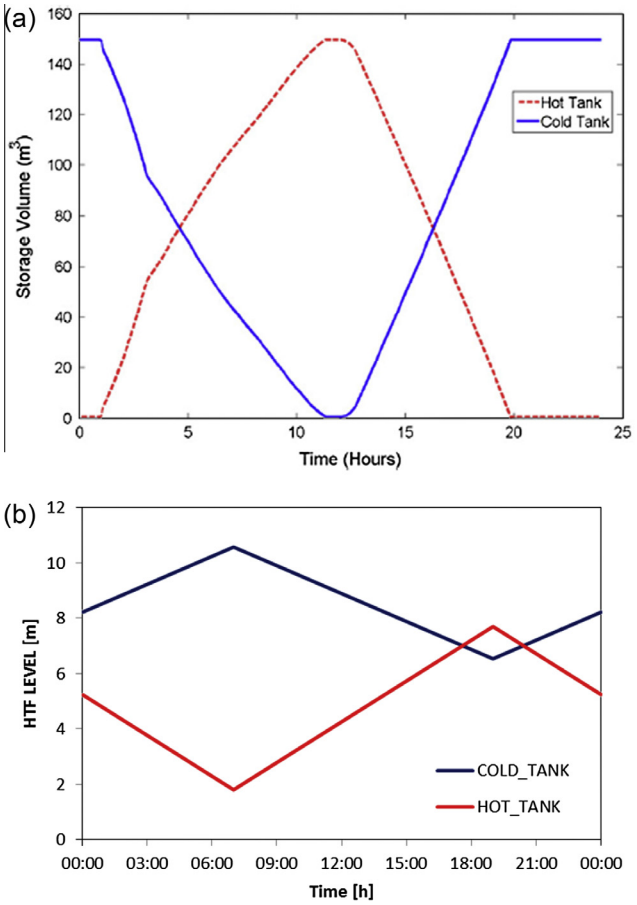

Fig. 5. Comparison of the modeled storages modeled by: (a) Powell and Edgar [24] and (b) the implemented model.

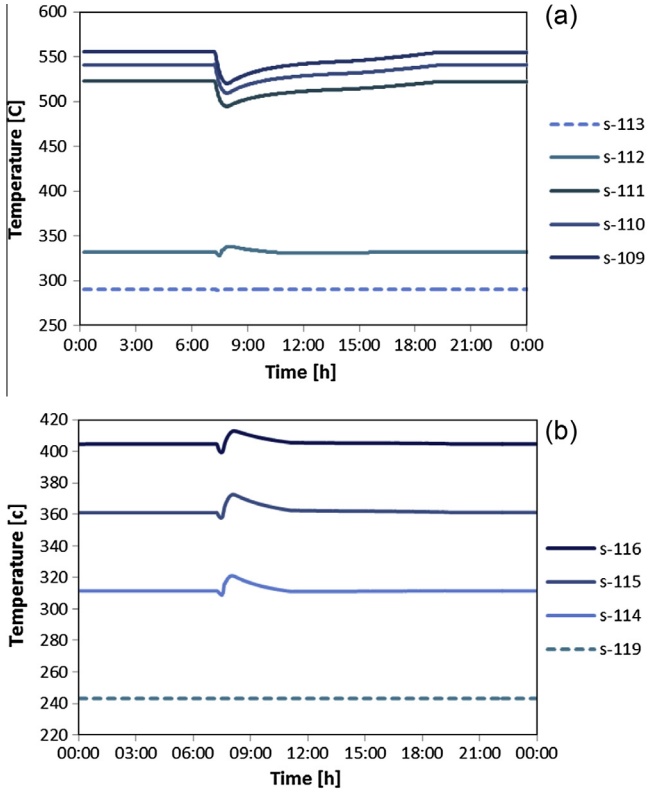

Fig. 6. The performance of HEX train, temperature of: (a) molten salt streams and (b) water/steam streams.

4. Low-temperature steam–biomass gasification

Biomass gasification is a thermo-chemical conversion in a reduced oxygen medium (partial oxidation), while the combustion takes place in the presence of (at least) stoichiometric oxygen. The common operating temperature for gasification is rather high, commonly varies from 750 °C to 1000 °C, depending on the type of feedstock and operating conditions [38,74,75]. The resulting products are fuel gases (mainly syngas, including interesting portions of carbon dioxide and methane) and slag, ash and solid residues are the by-products. Although, gasification is conceptually high-temperature process, it might be operated at relatively low temperature steam by adapting the effective parameters, operating conditions and alternative design options in the configuration of reactor. The main concern of this activity is to investigate and apply the low-temperature steam (~410 ° C) generated from the predesigned CSP plant, which is linked to biomass gasification process (Fig. 7) and drive it efficiently without any additional superheating supplied by fossil fuel.

In the acquaintance of the authors, low-temperature steam second gasification biomass has not yet been investigated in the literature so far. Hertwich and Zhang [76] proposed a work on the gasification process for a 3rd generation biofuel. However, in his work, the design was based on steam gasification of biomass with the heat supported by the means of solar tower technology directly, which provides heat at over 1000 °C and even not comparable with the concept of applied TES technology of the designed CSP plant in the current work.

4.1. Modeling of gasifier (R-301)

The Intra- and inter-phase heat and mass transfer phenomena must be considered coupled with detailed kinetics to obtain an effective model for biomass gasification, especially when thick biomass particles have to be processed. According to prior works [35,36], a convenient way to present the mass and energy balance equations is to distinguish the particle and the reactor scale. The particle model is able to predict temperature profiles and product distribution as the function of time. This model applies the reaction kinetics and also reliable rules for estimating transport properties to account for morphological changes during the pyrolysis process. Due to this, the intra-particle mass and heat transfer resistances are simply described by assuming an isotropic sphere. The particle is discretized into several sectors to characterize the temperature and concentration profiles, and the dynamic behavior of the particle under pyrolysis, gasification and combustion regimes. The gradients of temperature and volatile species inside the particle are evaluated by means of the energy and continuity equations, respectively N sectors are assumed to discretize the particle.

The mass balance of the solid phase is:

$$\frac{dm_{j,i}}{dt} = V_j R_{j,i}$$

where $m_{j,i}$ is the mass of the ith solid component; V_j is the volume of the jth sector; $R_{j,i}$ is the net formation rate of the ith component resulting from the multi-step devolatilization model and from the heterogeneous gas–solid reactions in the jth sector; finally, t is the time variable. The mass balance of the gas phase is:

$$\frac{dm_{j,i}}{dt} = J_{j-1,i}S_{j-1} - J_{j,i}S_j + V_j R_{j,i}$$

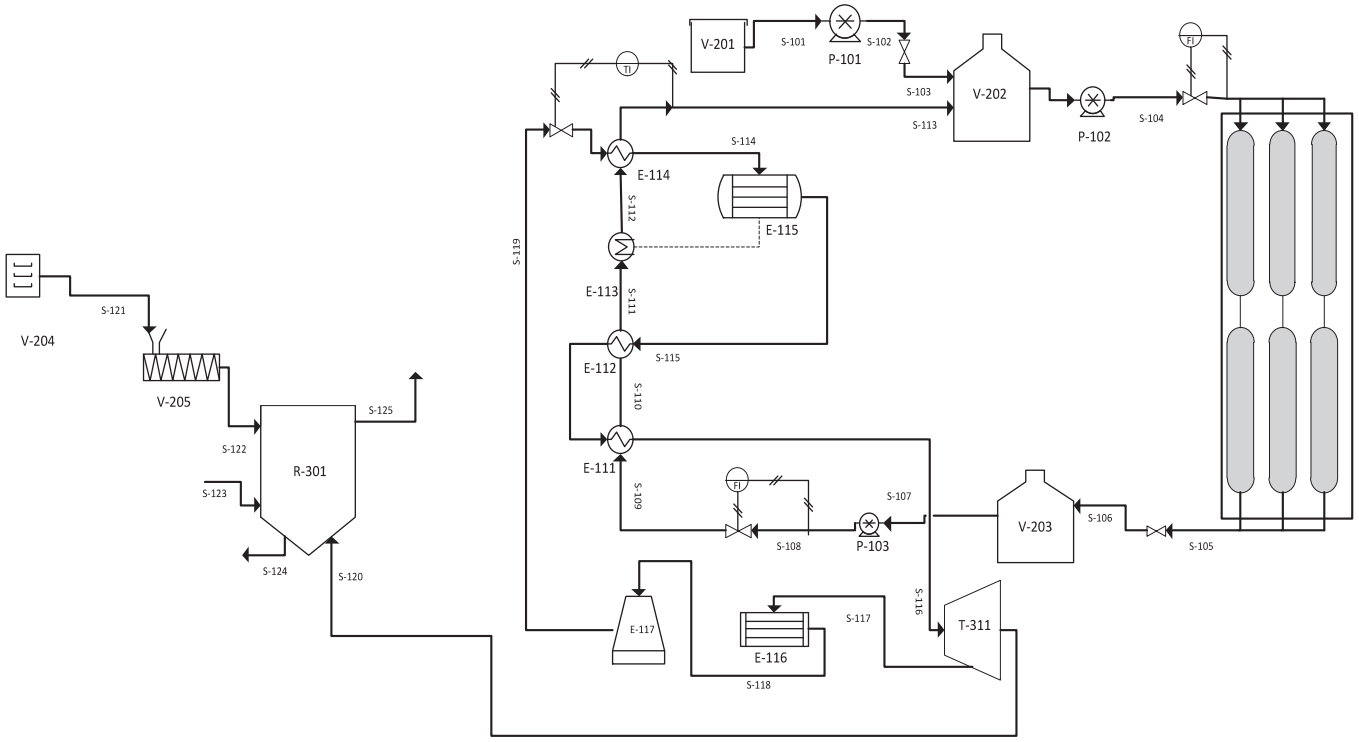

Fig. 7. Solar-driven biomass gasification process coupled to CSP plant.

where $m_{j,i}$ is the mass of the ith volatile species within the jth sector; S_j is the external surface of the jth sector; and J are the total fluxes generated by diffusion and pressure gradients. The energy balance is:

$$\frac{d\sum_{i=1}^{NOP} m_{j,i}h_{j,i}}{dt} = JC_{j-1}S_{j-1} - JC_jS_j + S_{j-1}\sum_{i=1}^{NOG} J_{j-1,j}h_{j-1,i} - S_j\sum_{i=1}^{NOG} J_{j,i}Cp_{j,i}T_j + V_jHR_j$$

where $h_{j,i} = c_{P_{j,i}}T_j$ is the component partial enthalpy; T_j is the temperature of the jth sector. The term JC accounts for the heat conduction; the term $V \cdot HR$ accounts for the total reaction heat; NCP is the total number of components; and NCG is the number of gas components. Mass exchange between adjacent sectors is only allowed for the volatile species, whereas solid compounds are constrained to remain inside the sector. The density profile inside the particle is evaluated as the sum of all the densities of different species $m_{j,i}$ present in each sector. Similarly, the shrinking and porosity of each sector are calculated. Mass and heat fluxes within the particle follow the constitutive Fick, Fourier, and Darcy laws:

$$J_{j,i} = -D_{j,i}^{eff}MW_i\frac{dc_{j,i}}{dr}\bigg|_{r_j} - \frac{\mathrm{Da}_j}{\mu_j}\frac{dP_j}{dr}\bigg|_{r_j} c_{j,i}MW_i$$

where $D_{j,i}^{eff}$ is the effective diffusion coefficient of the ith component inside the jth sector; MW and c are the molecular weight and the concentration; r is the radius; Da is the Darcy coefficient of the solid; μ is the viscosity of the gas phase; P is the pressure.

$$JC_j = -\kappa_j^{eff}\frac{dT_j}{dr}\bigg|_{r_j}$$

where κ_j^{eff} is the effective conduction coefficient inside the jth sector. The boundary conditions at the gas–solid interface become:

$$J_{N,i} = k_{ext}MW_i\left(c_{N,i} - c_i^{bulk}\right) + \frac{\mathrm{Da}_N}{\mu_N}\frac{\Delta P}{\Delta r}\bigg|_N c_{N,i}MW_i$$

$$JC_N = h_{ext}\left(T_N - T^{bulk}\right) + JR_N + \sum_i^{NCG} J_{N,i}h_{N,i}$$

where k_{ext} and h_{ext} are the convective transfer coefficients [77] and JR_N is the net radiation heat.

While the mathematical model of the fluidized bed or the entrained bed reactors can directly refer to the previous particle model, the modeling of fixed bed reactors takes advantage from the definition of an elemental reactor layer describing the gas–solid interactions. The solid bed is then simulated as a series of NR elemental layers. The height of each layer is of the same order of the size of the biomass particle, accounting for the vertical dispersion phenomena. The complete mixing inside the layer both for the gas and solid phase is assumed. The gas-phase mass balance equations for each elemental reactor are:

$$\frac{dg_i}{dt} = G_{in,i} - G_{out,i} + J_{N,i}S_N\eta + V_RR_{g,i}$$

where g_i is the mass of the ith species within the reactor volume V_R; $G_{in,i}$ and $G_{out,i}$ are the inlet and outlet flowrate; $R_{g,i}$ is the net formation from gas-phase reactions; the term $J_{N,i}$ is the gas–solid mass exchange multiplied by the particle surface S_N and η the number of particles inside the layer. The gas-phase energy balance equation for each elemental reactor is:

$$\frac{d\sum_{i=1}^{NCG} g_ih_{g,i}}{dt} = \sum_{i=1}^{NCG} G_{in,i}h_{gin,i} - \sum_{i=1}^{NGC} G_{out,i}h_{gout,i} + \sum_{i=1}^{NGC} J_{N,i}h_{N,i}S_N\eta + h_{ext}\left(T_N - T^{bulk}\right)S_N\eta + V_RHR_g$$

where $h_{g,i} = c_{P_i}T^{bulk}; T^{bulk}$ is the gas-phase temperature; the terms $G \cdot h_g$ are the enthalpies of inlet and outlet flow rates; the term $J \cdot h$ is the enthalpy flux relating to the mass transfer of a single particle; finally HR_g is the overall heat of gas-phase reactions.

4.2. Simulation of coupled gasification

The gasifier modeled is coupled to the pre-modeled CSP plant. This model is selected as a countercurrent fluidized bed gasifier with steam and oxygen as the oxidizers [75,76]. Indeed, using the countercurrent model for gasifier allows to the high tem-perature ashes to move down slowly to the bottom of the equip-ment and increasing the temperature of the steam supported from the bottom. In order to re-design the gasifier to adapt and couple it with low-temperature steam gasification, the effective parameters are needed to be considered to keep the efficiency of the process. These parameters are: operation conditions, con-figuration of the gasifier and, pretreatment of feedstock such as: the humidity of feedstock, size of the particle, equivalent ratio, and steam:biomass ratio. The overall specification and parameters to run the gasifier are summarized in Table 1.

The main challenge of this section is adjusting the temperature. The biomass gasification generally occurs at 650–1400 °C, whereas the steam (by CSP plant) to supply the gasification is around 410 °C (683 K). In other words, in this process, the temperature of steam is not a degree of freedom. Therefore, the other conditions and effective operation conditions should be investigated and determined and in case, re-designing the gasifier would be required to make the process comparable with high-temperature steam (conven-tional) gasification. Due to this, the effective parameters are con-sidered according to the overall basic operating condition adapted with low-temperature biomass gasification. As the objec-tive of the process is pursuing the methanol/DME synthesis plant, the ratio of H_2:CO is taken as a benchmark of efficiency of the pro-cess. Generally, the ratio of H_2:CO at high-temperature biomass gasification is almost unity. Therefore, it should be approached or compensated from another unit to keep the objectives of low-temperature process [78].

4.2.1. The effect of particle size

To investigate the effect of particle size on H_2:CO ratio in low-temperature gasification, two different sizes of particle (less and greater than 1 cm) for 5 mm and 2 cm were selected to conclude the discussion. Although different sizes of these ranges were modeled and considered for conclusion, it was attempted to bring only the above-mentioned sizes, since they generally obey the identical trend of behavior. The modeled particles show that by increasing the size of the particle, the heat transfer resistance in the layers increases, as it is shown in Fig. 8. In addition, the temperature of inner layers is not high enough to complete the pyrolysis and the secondary reaction of gasification and hence, the lower yield of hydrogen and the other species is observed (Fig. 9a). Moreover, with the trend of bulk temperature (Fig. 9b), it is concluded that a smaller size is under the control of kinetics, while heat and mass transfer on the surface of the particle affect the larger size.

It is worth mentioning that in order to avoid the diffusion problem in larger sized of particles, the particle was modeled in three-section layers to be comparable with one layer smaller size particles.

4.2.2. The effect of humidity of feedstock

Biomass contains a high amount of moisture in its structure in addition of other components such as carbon, hydrogen, and oxygen [38]. The high amount of moisture in fuel uses the energy of gasification and as a result, decreases the temperature of the gasification process and consequently, becomes an inefficient process. Therefore, it is necessary to decrease the content of water, especially for low-temperature gasification, which is needed to preserve the energy especially to avoid consuming it on drying the feedstock up. Thus, the pre-treatment process is required to dry the feedstock before feeding it into the gasifier. Due to this, the optimum amount of moisture allowed to be applied in the contents of feedstock is required to be determined. This is more critical especially at a higher percentage of humidity as it is shown in Fig. 10. By decreasing the humidity, the efficiency of the plant in terms of H_2:CO is increased. For the humidity of less than 10%, the ratio of H_2:CO is almost constant. Considering the crucial range, it would help to preserve the extra energy, neither having high content of moisture in feedstock nor drying more than what is required.

Table 1
The overall operational conditions for modeled low-temperature process.

Biomass	
Ultimate analysis	Unit (wt.%)
C	51
H	6.1
O	42.9
Particle specification	Unit
Density	1250 kg/m^3
Porosity	30%
Humidity	7%
Diameter	8 mm
Reactor	
Surface	3 m^2
Height	4 m
Flow rate of biomass	47,000 kg/h
Bulk	
Oxidizer	
Oxygen	10%
Steam	90%
Syngas	Unit (mol.%)
H_2	6.2
CO	8.7
CO_2	8.8
H_2O	71
CH_4	2.0
Solid residue	Unit
Gravity	5.2%
Residue	2444 kg/h
Ash	2%

4.2.3. The effect of component of feedstock

As it is obvious, the three main well-known components of biomass are cellulose, hemicellulose and lignin [36,70]. Lignin is a highly cross-linked polymer of methoxy- and phenoxy-substituted phenyl propane units. Cellulose is a complex polymer of glucose and hemicellulose is of various sugar units [35,36,79]. In this section, the general component of biomass is applied as dominant on its structure. In order to understand this, two general kinds of biomass are simulated as shown in Table 2.

Cellulose-based biomass is the usual type of biomass where the content of cellulose is dominant and the amount of it is higher than the other two constituents, i.e., lignin and hemicellulose (Table 2). Lignobiomass is the lignin based biomass with higher amount of lignin in its content. It is worth mentioning that this type of biomass is the by-product of separation process after distillation of ethanol (PROESA® Technology).

Lignin has a generally lower oxygen content and higher carbon content as compared to cellulose, hemicellulose [35,36,79]. Owing to this fact, the characteristic of the biomass tends is similar to carbon-based feedstock and, therefore, the yield of hydrogen is higher than cellulose based feedstock. This feature provides the possibility of producing a higher ratio of H_2:CO in comparison with cellulose based composition (Fig. 11).

4.2.4. The effect of equivalent ratio

Another operating condition influencing the efficiency of the gasification, is equivalence ratio (ER). ER is defined as the actual oxygen to biomass ratio divided by the stoichiometric oxygen to

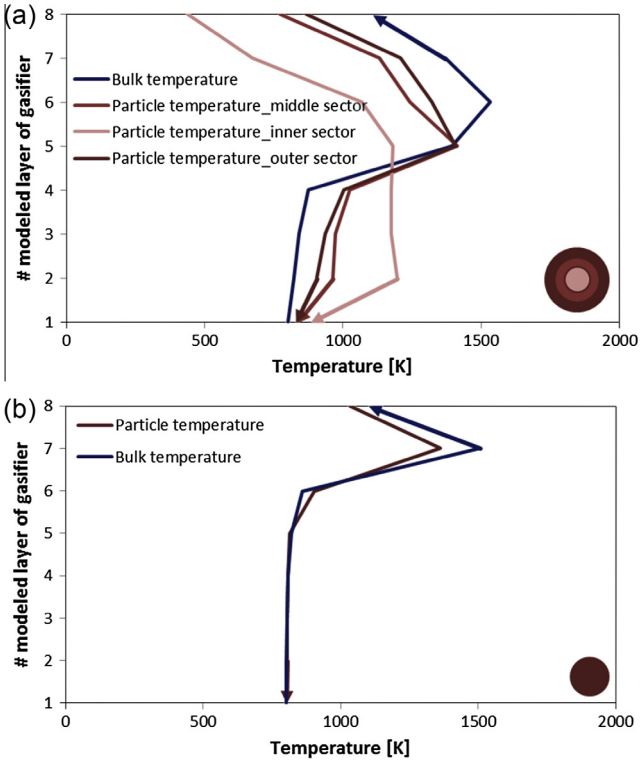

Fig. 8. The effect of particle size in low-temperature gasification: temperature of bulk and particle for: (a) 2 cm (three layers modeled) and (b) 5 mm (one layer modeled).

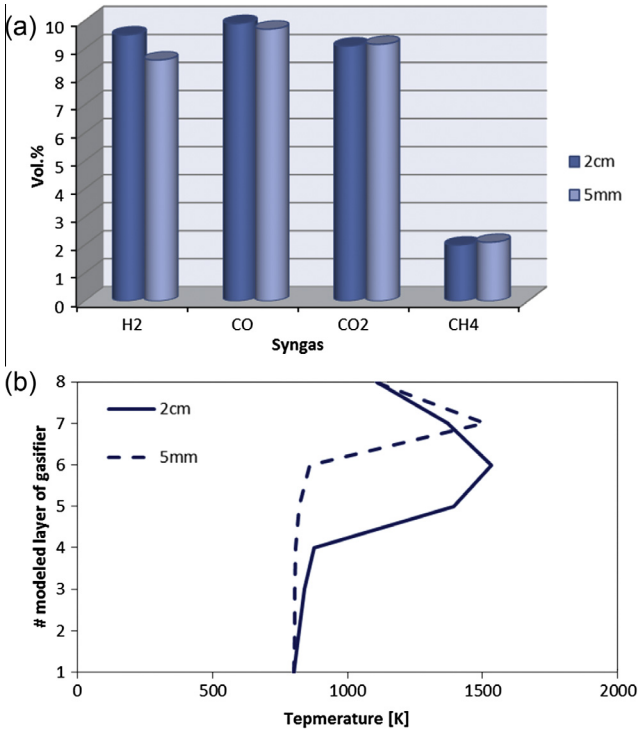

Fig. 9. The effect of particle size in low-temperature gasification: (a) the composition of the produced gases in different sizes and (b) comparison of bulk temperature in different sizes.

biomass ratio [37,80]. This term is crucial because the high value of ER results in a lower concentration of H_2 and CO as well as in a higher CO_2 content of produced gas, due to the more combustion governed on gasification.

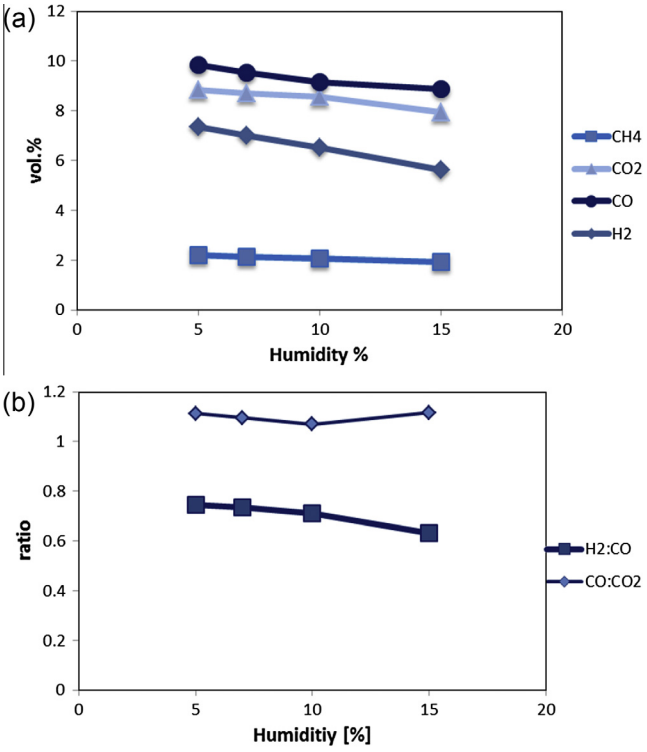

Fig. 10. The effect of humidity on: (a) produced gases and (b) H_2:CO ratio.

As it is observed (Fig. 12), the amount of residue in production decreases in the similar trends for lower temperatures, and the content decreases obviously by increasing in the temperature (Fig. 12a). Increasing ER (or decreasing λ) increases the ratio of H_2:CO, as it is seen in Fig. 12b. The optimum amount is found at λ = 0.25 for the desired temperature (683–700 K), as it is highlight-ed in Fig. 12, which presents approximately 6.5% of solid residue in production. It is worth noting in higher ER (lower λ) at 600 K (Fig. 12b), the yield of H_2 is abruptly decreased since the tem-perature is extremely low. Therefore, it causes unexpected shut-down of the process, which is shown as a sharp decreasing of ratios of H_2:CO. However, the operation applied to the proposed and modeled gasifier is used at 683–700 K with λ = 0.2, which is in agreement with other discussed parameters.

4.2.5. The effect of residence time

Residence time influences the gasification process strongly. When relying on multi-phase interaction of a gas–solid nature of gasification, it is necessary to provide appropriate residence time for interaction between bulk and particle. Agreeing on the inverse relationship of residence time and flowrate of the feedstock, increasing the flowrate in identical volume of gasifier decreases the residence time and this causes an inefficient gasification and consequently, increased amount of residue in the production.

As it is shown in Fig. 13, the effect of residence time is more tangible at lower temperature, while at higher temperatures this effect is no longer operative. As a result, by increasing the residence time in lower feedstock, the efficiency of the process increase, i.e., H_2:CO increases. Indeed, the increased value is higher for the high-temperature operation than for the lower-temperature one. Since the desired temperature for this activity is at 683–700 K, the ratio around 0.8 is considerable (Fig. 13).

4.3. Re-designing the gasifier

Decreasing the solid residue as a benchmark of efficiency motivates the concept of re-designing the gasifier for the purpose of a

Table 2
The component of modeled biomass.

Component (wt.%)	Cellulose	Hemicellulose	Lignin C*	Lignin H*	Lignin O*	Ash
Cellulose-based biomass	40	20	5	25	8	2
Lignobiomass	35	8	30	20	5	2

Lignin C, Lignin H and Lignin O represent their characteristic of being richer in carbon, hydrogen, and oxygen, respectively [30].

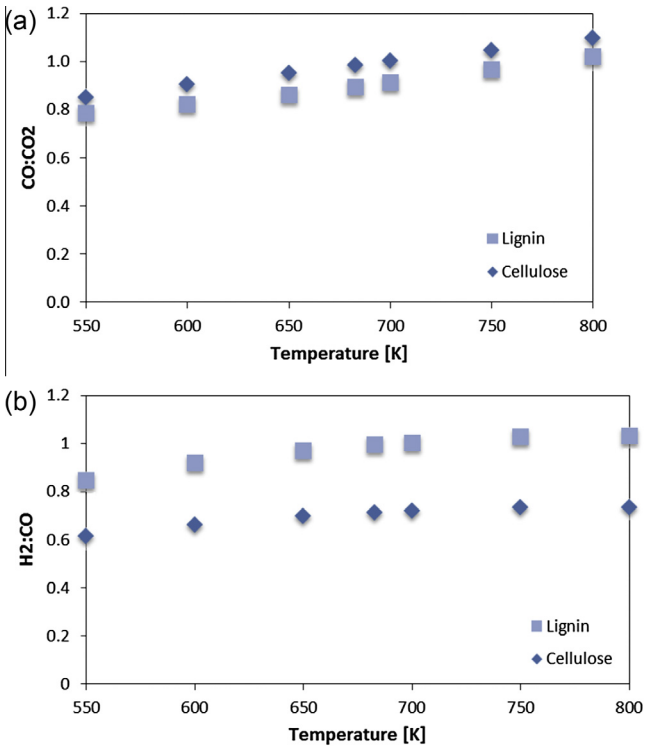

Fig. 11. The effect of component on: (a) CO:CO_2 ratio and (b) H_2:CO ratio.

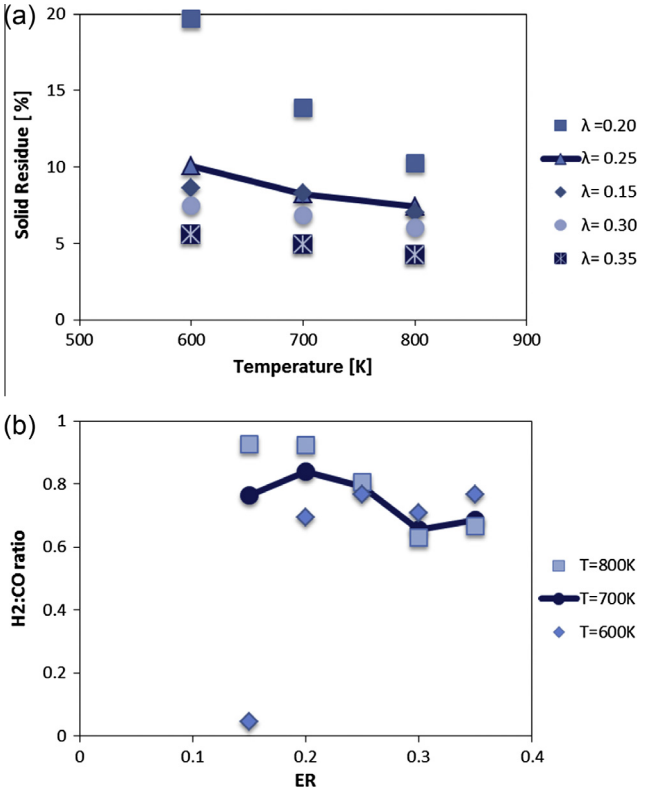

Fig. 12. The effect of λ (1/ER) on: (a) solid residue and (b) H_2:CO ratio.

low-temperature (700 K) process, and at similar operating conditions. Two different cases for re-designing the gasifier are opted and aim at reducing the amount of residue it takes by varying the amount of oxygen supported to the gasifier and increasing the height (volume) of reactor, and consequently the residence time. As it is seen, by increasing the amount of injected oxygen to the gasifier, the efficiency of the gasification is increased (Case A). In addition, providing more residence time for biomass particles (increasing the volume of gasifier for identical operating conditions) would meet the efficiency of the gasification process (Case B). For this purpose, it was attempted to model both cases consid-ering the economic evaluation of each case, and therefore, the proper decision making is needed to re-design the low-temperature gasifier with respect to the discussed operating condi-tions. Due to this, the performance of each case is evaluated regarding 1% decreased amount of solid residue.

As it is observed (Fig. 14a), increasing the height of the gasifier, which is equal to increasing the residence time, will increase the effi-ciency of the process in comparison with the lower height of the reactor. The designated amount of residue decreased (1%) occurs at a 2 m increased height of the gasifier. However, Case B an increased amount of oxygen (0.288 Nm^3/s) is needed, in comparison with base operating condition (Fig. 14b). The equivalent ratio and feedstock flowrate both are kept at 0.2 and 47,000 kg/h, respectively.

Cost evaluation for both modeled cases illustrated the efficiency of applying the larger gasifier. The economic calculations demonstrate that the cost of supplying extra oxygen is annually 1.375% times more than of that of replacing a larger gasifier to the plant (Table 3). In conclusion, to manage the operation for low-temperature gasification process, it is vital to re-design the adapted reactor for the plant.

5. Methanol/DME plant

The syngas obtained in the gasification process (V-301) is fed to the methanol/DME synthesis (Fig. 15). A steam reforming reactor (R-302) could be accounted before the methanol/DME synthesis for converting the fraction of methane generated in the biomass gasification. The series of reactors (R-303, R-304, V-208 and V-209) applied through this pathway has been modeled in C++ and integrated with the simulation suite PRO/II. Moreover, the syngas coming from gasification (V-301), which composition is reported in Table 4, could undergo an adjustment of H_2/CO ratio by a water gas shift (WGS) reactor with the aim of increasing the hydrogen content. This process is crucial for the majority of the chemical processes that use syngas as feedstock; it could be skipped in the scheme proposed in this paper since the WGS is directly active on the catalyst for methanol synthesis and it takes place in situ. In any case, also the WGS reactor is taken into consideration in the present work to extend the generality of the proposed scheme toward different energy carriers and chemical commodities.

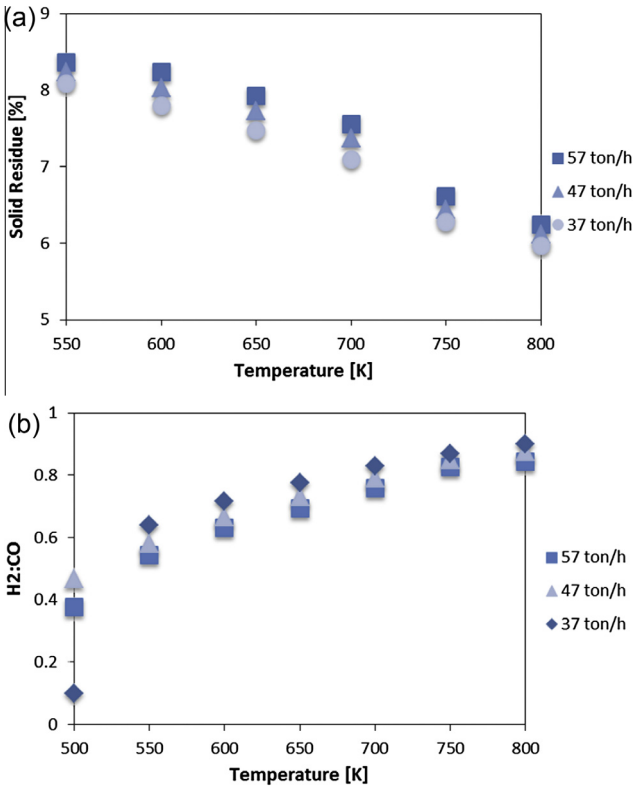

Fig. 13. Effect of residence time on: (a) solid residue and (b) H_2:CO ratio.

A relevant simplification of the proposed layout rely in the absence of gas sweetening units for the sequestration of CO_2 or H_2S, generally produced in coal gasification systems. The exclusion of sweetening processes is related to the assumptions of having a biomass feedstock with negligible sulfur content. At last, the gasification process is supposed to be supplied by pure oxygen instead of air, with the possibility to skip any nitrogen separation before the methanol synthesis.

By doing so, syngas is conducted into the water gas shift/steam methane reforming reactor (R-302) to recover and promote the amount of the hydrogen and carbon monoxide. Although hydrogen yield in the syngas produced from non-catalytic biomass gasification is generally low, the amount of hydrogen can be however increased by converting CO, CH_4, higher hydrocarbons, and tar in a secondary reactor. The enrichment based on 6820 kmol/h of syngas (Table 4) at 650 °C and 30 bar is given by the two overall following reactions:

$$CH_4 + H_2O \leftrightarrows CO + 3H_2 \quad \Delta H = 206\ \text{kJ/mol}$$

$$CH_4 + 2H_2O \leftrightarrows CO_2 + 4H_2 \quad \Delta H = 165\ \text{kJ/mol}$$

The composition of enriched syngas is given in Table 5. In addition, the water gas shift reaction active in the methanol/DME synthesis reactor leads toward the in situ consumption of CO_2 without the need of removal units.

5.1. Methanol/DME synthesis

As it is known, the production of methanol and DME are accomplished under catalytic conversion [49] of syngas. The synthesis takes place in a reactor at high pressure. Methanol is produced from H_2 and CO via reaction (a) as well as it could be produced from H_2 and CO_2 through the reaction (b), although reverse water gas shift (c) is faster in converting CO_2 into CO for favoring the reaction (a):

$$\text{Methanol synthesis reaction:}\quad 2H_2 + CO \leftrightarrows CH_3OH \quad \Delta H = -181.6\ \text{kJ} \tag{a}$$

$$\text{Alternative methanol synthesis reaction:}\quad 3H_2 + CO_2 \leftrightarrows CH_3OH + H_2O \quad \Delta H = -49.43\ \text{kJ} \tag{b}$$

$$\text{Water gas shift (WGS) reaction:}\quad H_2O + CO \leftrightarrows CO_2 + H_2 \quad \Delta H = -41.0\ \text{kJ} \tag{c}$$

These reactions are dependent on each other and each of them can be expressed as a linear combination of the other as indicated in other works [84,85]. An exothermic condition is favored at low temperature despite the reaction rate; moreover, it is necessary to operate at high pressure (for instance; 80 bar) to improve the equilibrium conversion exploiting the reduction in number of moles. Typically, synthesis of methanol is conducted over commercial catalyst $CuO/ZnO/Al_2O_3$, which has an estimated 3–4 years lifetime [49]. Since catalyst deactivation occurs at temperatures above the 550 K, the operating range of temperature is 500–540 K [86,87]. On the other hand, the operating pressure is at 50–100 bar for commercial synthesis and typical operating pressure is at 50 bar for DME synthesis (at ~530–540 K). Therefore, the operating condition is selected at 540 K and 50 bar, compromising for both chemicals. Traditionally, DME production has been based on gas auto reformation or coal gasification. Two-step DME synthesis is the main process used, which includes separate steps of methanol synthesis and methanol dehydration:

$$\text{Methanol dehydration (DME synthesis):}\quad 2CH_3OH \leftrightarrows C_2H_6O + H_2O \quad \Delta H = -23.4\ \text{kJ} \tag{d}$$

$$\text{Direct synthesis of DME:}\quad 4H_2 + 2CO \leftrightarrows C_2H_6O + H_2O \quad \Delta H = -205\ \text{kJ} \tag{e}$$

$$\text{Direct synthesis of DME (combined reaction):}\quad 3H_2 + 3CO \leftrightarrows C_2H_6O + CO_2 \quad \Delta H = -246.0\ \text{kJ} \tag{f}$$

Recently, one-step technologies has been developed to combine methanol synthesis and methanol dehydration in one single reactor pass [88]. DME is produced by dehydration of methanol (d). The production of DME can take place based on methanol or, directly from a syngas through the reactions ((a) and (d)), which gives the reaction in (e). However, the combination of the reaction (d) and (c), could provide more effective total reaction (f), which is the production of the water in dehydration of methanol to synthesis DME (d).

The resulting process is called direct DME synthesis and employs a bifunctional catalyst composed by the already known $CuO/ZnO/Al_2O_3$ for methanol synthesis coupled with γ-Al_2O_3 for the methanol dehydration. The phenomena occurring in the first portion of the reactor (first 1–2 m along the reactor) is kinetically limited, while in the further part the chemical equilibrium plays a major role limiting the reaction. In the first part, a point with maximum temperature is developed called temperature hot-spot. Controlling the hot-spot is critical to improve the process efficiency and, also to preserve the catalyst activity, process safety and some special techniques required to monitor it [89–92].

The outflow of the water cooled reactor (R-303) is fed to tube side of gas-cooled reactor (R-304), where methanol is synthesized. The temperature of the reactor is controlled by the temperature of the boiling water (V-303). On the other hand the temperature profile of the reactor (R-304) is controlled by exchanging with fresh

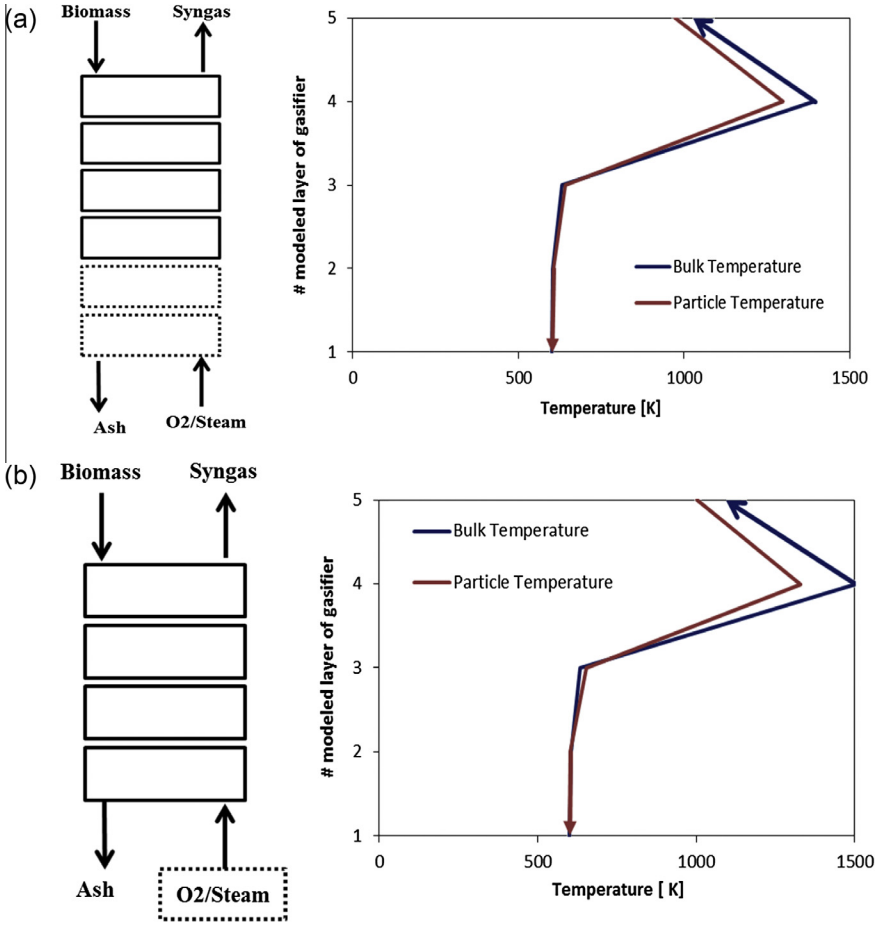

Fig. 14. Re-designing the low-temperature gasifier for: (a) increased height of reactor and (b) increased amount of oxygen.

Table 3
The economic evaluation of proposed cases.

	Oxygen cost ($/mol.%)	Gasifier cost ($/m^3)	Reference cost estimation equation	Cost per 1% decreased residue ($/year) 2012	Reference year for cost
Case A	0.07	–	–	61699.9	2010[a]
Case B	–	15,000	[b]$C_2 = C_1 \cdot (S_1/S_2)^{0.6}$	44862.5	2004[a]

[a] The cost is correlated according to "cost (year 2012) = cost (Ref. year). ($CI_{2012}/CI_{Ref.year}$)" [81,82].

[b] S_1 and S_2 are the size of equipment; C_1 and C_2 are the rapid capital costs [83].

inlet syngas (V-301) to be pre-heated in counter-current of shell side. The outflow of R-304 is then, sent to the downstream process, where methanol is recovered and also, unreacted syngas is recycled back. Meanwhile, a purge system is applied to remove by-products, and accumulations of incondensable gas(s). The detail of the modeled reactors is described in the following section.

5.2. Modeling of methanol/DME reactor (R-303, R-304)

The mathematical modeling of the overall system can be divided into three main components: (i) the model of R-303; (ii) the model of R-304; and (iii) the preliminary phase separation (V-208) for syngas recycle from the raw methanol. The mathematical model developed for simulation of methanol production loop is based on the assumption of negligible axial and radial diffusion [92], constant radial velocity, constant temperature and pressure profiles within the catalytic pellet, negligible catalyst deactivation and side reactions, and catalytic particle efficiency using modified Thiele modulus:

$$\phi_i = \frac{r_P}{3}\sqrt{\frac{k_j'\left(k_j^{eq}+1\right)}{\mathcal{D}_e^j k_j^{eq}}}$$

$$\eta_i = \frac{1}{\phi_i}\frac{(3\phi_i \coth(3\phi_i) - 1)}{3\phi_i}$$

where ϕ_i is the modified Thiele modulus, r_P is the radius of the catalytic pellet, k_j' is the pseudo-first-order constant of the jth reaction, k_j^{eq} is the equilibrium constant of the jth reaction; $\mathcal{D}_e^j$ is the effective diffusivity of the jth component of the mixture as specified by Lommerts et al., [93]. The linearized kinetics required to derive k_j' for methanol and water are, respectively:

$$r'_{CH_3OH} = k_j' \quad C_{H_2} - \frac{C_{CH_3OH}}{k_{CH_3OH}^{eq}}\Bigg)$$

$$r'_{H_2O} = k_j' \quad C_{H_2} - \frac{C_{H_2O}}{k_{H_2O}^{eq}}\Bigg)$$

The kinetic rates are obtained by replacing r, k_{eq} and concentration values calculated at the integration step. The kinetic laws adopted were already proposed elsewhere [94,95]:

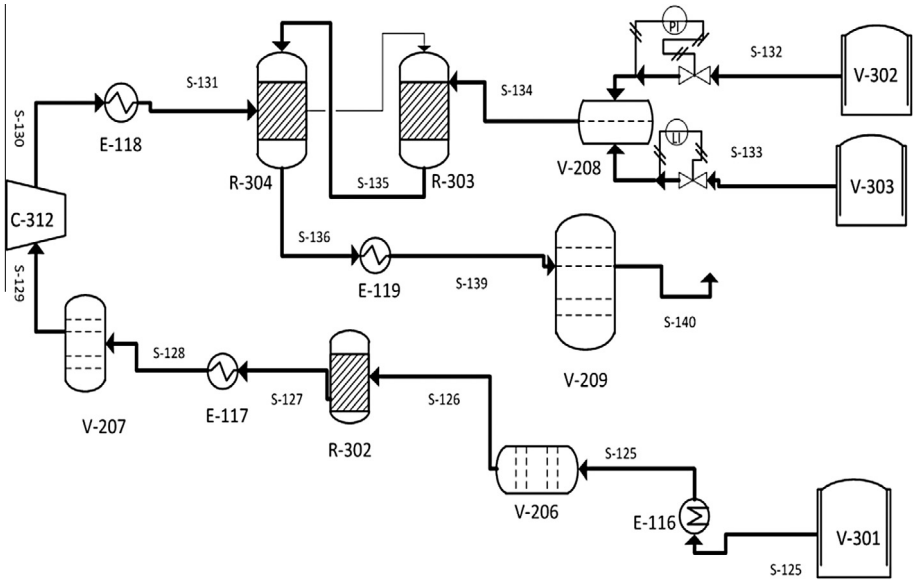

Fig. 15. Molded methanol/DME synthesis process.

Table 4
Composition of produced syngas (V-301).

Flowrate	kmol/h	6820
Composition (%) dry basis	H_2	24.1
	CO	34.2
	CO_2	33.8
	CH_4	7.7

$$r_1 = \frac{k_1 K_{CO}\left[f_{CO} f_{H_2}^{1.5} - \frac{f_{CH_3OH}}{f_{H_2}^{0.5} K_{P1}}\right]}{(1 + K_{CO} f_{CO} + K_{CO_2} f_{CO_2})\left[f_{H_2}^{0.5} + \left(\frac{K_{H_2O}}{K_{H_2}^{0.5}}\right) f_{H_2O}\right]}$$

$$r_2 = \frac{k_2 K_{CO_2}\left[f_{CO_2} f_{H_2} - \frac{f_{CO} f_{H_2O}}{K_{P2}}\right]}{(1 + K_{CO} f_{CO} + K_{CO_2} f_{CO_2})\left[f_{H_2}^{0.5} + \left(\frac{K_{H_2O}}{K_{H_2}^{0.5}}\right) f_{H_2O}\right]}$$

$$r_3 = \frac{k_3 K_{CO_2}\left[f_{CO_2} f_{H_2}^{1.5} - \frac{f_{CH_3OH} f_{H_2O}}{f_{H_2}^{1.5} K_{P3}}\right]}{(1 + K_{CO} f_{CO} + K_{CO_2} f_{CO_2})\left[f_{H_2}^{0.5} + \left(\frac{K_{H_2O}}{K_{H_2}^{0.5}}\right) f_{H_2O}\right]}$$

The most common way to consider the production of dimethyl ether when employing a bifunctional catalyst is to couple two kinetic models, one for the synthesis of methanol and another for the methanol dehydration described in [96]:

$$r_4 = \frac{k_4 K_{CH_3OH}^2 \left(C_{CH_3OH}^2 - \frac{C_{H_2O} C_{DME}}{K_{C4}}\right)}{\left(1 + 2(K_{CH_3OH} C_{CH_3OH})^{1/2} + K_{H_2O} C_{H_2O}\right)^4}$$

Table 5
Composition of enriched syngas.

Flowrate	kmol/h	6820
Composition (%) dry basis	H_2	49.15
	CO	10.51
	CO_2	37.4
	CH_4	2.93

The gas-cooled and water-cooled reactors are modeled assuming the concentration and temperature gradients of gas–solid phases are negligible, significantly simplifying the numerical solution and reducing the computation time stabilizing the accuracy [52]. Constitutive equations for the water-cooled reactor model are:

Mass balance

$$\frac{M}{A_{int}} \frac{d\omega_i}{dz} = MW_i \rho_{cat} (1 - \varepsilon_b) \sum_j^{NR} v_{ij} \eta_j r_j$$

Water-cooled and gas-cooled energy balance:

$$\frac{M c_{p_{mix}}}{A_{int}} \frac{dT_c}{dz} = \pi \frac{d_{int}}{A_{int}} U (T_{shell} - T_{bulk}) + \rho_{cat} (1 - \varepsilon_b) \sum_j^{NR} \left(-\Delta H_j^{rxn}\right) \eta_j r_j$$

Ergun equation

$$\frac{dP}{dz} = -\left(1.75 + 150\left(\frac{1 - \varepsilon_b}{\mathrm{Re}}\right)\right) \frac{u^2 \rho_{gas}}{d_p} \left(\frac{1 - \varepsilon_b}{\varepsilon_b^3}\right)$$

Equations are the equal for gas-cooled reactor; however, the additional energy balance to characterize the coolant gas flowing in countercurrent is required. The energy balance for the shell side of the gas-cooled reactor is:

$$\frac{M c_{p_{mix}}}{A_{int}} \frac{dT_c}{dz} = -\pi \frac{d_{int}}{A_{int}} U (T_c - T_{shell})$$

Eventually, the preliminary separation of the syngas recycle consists of a simple flash drum separator, the total component mass balances are:

$$F = V + L$$

$$Fz_i = Vy_i + Lx_i$$

$$\sum_{i=1}^{N} y_i = 1$$

$$\sum_{i=1}^{N} x_i = 1$$

Given flash separator conditions, the solution is found adopting the method proposed in [97]:

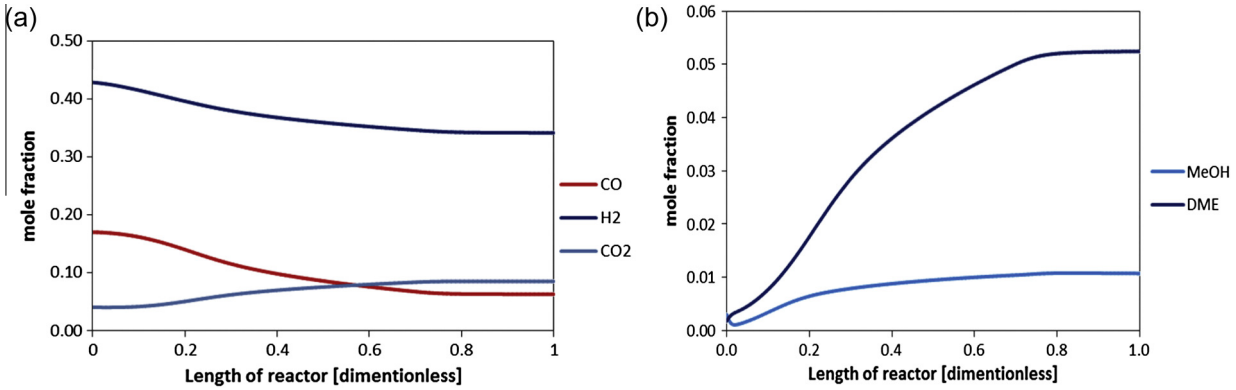

Fig. 16. Methanol/DME reactor: (a) syngas composition in products after synthesis and (b) composition of produced methanol and DME.

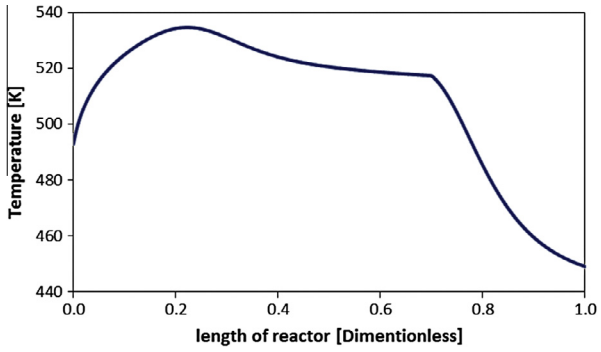

Fig. 17. Profile of the temperature of tube side through methanol/DME synthesis reactor.

$$f(V/F) = \sum_{i=1}^{N} \frac{z_i(K_i - 1)}{\frac{V}{F}(K_i - 1) + 1} = 0$$

where K_i are K-values and were calculated using and appropriate equation of state:

$$K_i = \frac{y_i}{x_i} = \frac{\phi_i^L}{\phi_i^V}$$

The syngas is fed to the shell side of the gas-cooled reactor, where it is pre-heated by the hot stream flowing in the tube side filled by catalyst, where the synthesis reaction takes place. The pre-heated syngas is then fed to the catalytic bed for methanol conversion and, specifically, to the tube side of water-cooled reactor. The methanol synthesis is particularly exothermic and the shell side is filled by boiling water to preserve the desired operat-ing conditions of water-cooled reactor. It is worth remarking that the temperature profile inside the methanol synthesis reactor is characterized by a hot spot [86], which must be subject to strict controls to prevent possible methanation reactions. The intrinsic intensified nature of the modern methanol process allows combining the conversion of methanol to the medium pressure steam generation. The 6820 kg/h feed composition (syngas) resulted from adjusted steam reforming section is implemented for methanol reactor as (in molar fraction): CO = 0.1048; CO_2 = 0.36; H_2 = 0.48; H_2O = 0.037; CH_4 = 0.0182.

The results of the simulation are reported in Fig. 16. The ratio of H_2:CO in the product composition has been decreased in comparison with this ratio in the entrance of the reactor due to the relative reactions, which were provided the methanol and DME (Fig. 16a). The temperature should not be higher than ~550 K, which is the threshold to prevent catalyst sintering as well as very exothermic side reactions (e.g., methanation) As it is seen in Fig. 16b, the production of DME is much higher than methanol due to the reactions (d, e, f). It is worth noting that the amount of DME could be controlled in the process by decreasing the ratio of H_2:CO (as it needs the ratio ~1) whereas the syngas enters into the reactor according to the reactions ((e) and (f)) and it would give the possibility of separating the H_2 stream as a valuable component for other applications. The temperature of the reactor (Fig. 17) is controlled by the temperature of the boiling water (V-303). In general, the first 70% of the total length is water-cooled reactor; the remaining part is the gas-cooled reactor, although different studies have been performed on this element in the recent literature [98].

The effluent of the methanol/DME synthesis reactor contains unreacted syngas (H_2, CO, CO_2, H_2O) besides methanol/DME. The conventional method for separation of methanol/DME from the gaseous components in the product gas is by cooling the product gas until the condensation of methanol/DME. In the case of methanol, condensation can be achieved with cooling the water, while the refrigeration of the product gas is needed for DME. After condensation, the steam is sent to a gas–liquid separator. The most of the gas is typically recycled back to the methanol/DME synthesis reactor, while the liquid stream is sent to the distillation column.

6. Conclusions

Following the definition and concept of the process integration, which is generally determined to design and unify the process via interaction between various unit operations, plants in operation, and energy connections, this activity was aimed and fulfilled in this direction to provide the feasibility of an innovative pathway of different sources of energy and units effectively. The concept of minimizing the cost and energy consuming through the process in the definition of process integration for this case study might be considered for further investigation by the authors or interested researchers in this field. In general, this work presented and demonstrated the feasibility of an innovative green pathway of synthesis of methanol/DME in one step from low-temperature steam biomass gasification. In the first step of this work, the concentrating solar power plant was modeled, simulated, optimized in order to generate the constant power throughout the 24-h of a day in spite of intermittent nature of solar. Afterward, the low-temperature-steam is applied to drive the biomass gasification process, which was needed to investigate and demonstrate the feasibility of low-temperature condition for the further unit. Therefore, all effective conditions such as: pre-treatment of feedstock, re-designing the gasifier were taken into account as the effective operating conditions. In this step, this green route produced syngas, is integrated into the methanol plant to synthesis methanol/

DME. In addition, overcoming on the complexity of design and integration of mentioned units in different software tools was the other remarkable achievement of this activity. Integrating the process in less energy-intensive and clean route was the other approach of this work to demonstrate the potential of renewable energies coupled with traditional units and processes. Therefore, this achievement into new models, simulation tools and information consistency as well, for this innovative pathway for biomass to energy carriers provided the feasibility of the entire plant from academy scale and gives the opportunity to extend in an industrial scale. Open issues are still the global optimization and energy integration of the utilities as well as the possibility to consider different technologies (for instance, different TES technologies in the CSP) and process lines (for instance, the possibility to recover pure hydrogen) to make the overall system further appealing.

Acknowledgments

The work is part of the BIOREFILL (BIORERefinery Integrated Lombardy Laboratories) project funded by Fondazione CARIPLO and Regione Lombardia. Authors gratefully acknowledge funding institutions above as well as the constant support of the Sustainable Process Engineering Research (SuPER) team staff (http://super.chem.polimi.it), where the project details are available. Specifically, modeling and simulation support by Professor Sauro Pierucci, Professor Eliseo Ranzi, Ing. Michele Corbetta, and Ing. Andres R. Leon-Garzon is acknowledged.

References

[1] Douglas MJ. Conceptual design of chemical process. NY: McGraw-Hill; 1988.
[2] El-Halwagie MM. Process integration. Boston: Academic Press; 2006. ISBN-13: 9780123705327.
[3] Towler G, Sinnot R. Integrated chemical engineering design. Butterworth-Heinemann; 2008. ISBN: 9780750684231.
[4] El-Halwagie MM. Process integration. Academic Press; 2006. ISBN-13: 9780123705327.
[5] Kemp IC. Pinch analysis and process integration. Elsevier; 2007. ISBN-13: 9780750682602.
[6] Siirola JJ, Edgar TF. Process energy systems: control, economic, and sustainability objectives. Comput Chem Eng 2012;47:134–44.
[7] Klemeš JJ, Varbanov PS, Pierucci S, Huisingh D. Minimising emissions and energy wastage by improved industrial processes and integration of renewable energy. J Clean Prod 2010;18:843–7.
[8] Wooruff EB, Lammers HB, Lammers TF. Steam plant operation; 2011. ISBN-13: 9780071667968.
[9] Kitto JB, Stultz SC. Steam: its generation and use. 41st ed. USA: The Babcock & Wilcox Co.; 2005. ISBN: 0963457012.
[10] Suomalainen MS, Arasto A, Teir S, Siitinen S. Improving a pre-combustion CCS concept in gas turbine combined cycle for CHP production. Energy Procedia 2013;37:2327–40.
[11] Memon AG, Harijan K, Uqaili MA, Memon RA. Thermo-environmental and economic analysis of simple and regenerative gas turbine cycles with regression modelling and optimization. Energy Convers Manage 2013;76:852–64.
[12] Berstad D, Anantharaman R, Nekså P. Low-temperature CCS from an IGCC power plant and comparison with physical solvents. Energy Procedia 2013;37:2204–11.
[13] Sorgenfrei M, Tsatsaronis G. Design and evaluation of an IGCC power plant using iron-based syngas chemical-looping (SCL) combustion. Appl Energy 2014;113:1958–64.
[14] Tokimatsu K, Tsuboi S, Iritani J, Onozaki M. Costs and performance of advanced zero emission systems of IGCC with CCS in Japan. Energy Procedia 2013;37:2519–28.
[15] Huang Y, McIlveen-Wright D, Rezvani S, Wang YD, Hewitt N, Williams BC. Biomass co-firing in pressurized fluidized bed combustion (PFBC) combined cycle power plant: a techno-environmental assessment based on computational simulations. Fuel Process Technol 2006;87:927–34.
[16] Andries J, Becht JGM, Hoppesteyn PDJ. Pressurized fluidized bed combustion and gasification of coal using flue gas recirculation and oxygen injection. Energy Convers Manage 1997;38:117–22.
[17] Kuravi S, Trahan J, Goswami Y, Rahman M, Stefanakos EK. Thermal energy storage technologies and systems for concentrating solar power plants. Prog Energy Combust Sci 2013;39:285–319.
[18] Manenti F, Ravaghi-Ardebili Z. Dynamic simulation of concentrating solar power plant and two-tanks direct thermal energy storage. Energy 2013;55:89–97.
[19] Lam HL, Klemes JJ, Kravanja Z, Varbanov PS. Software tools overview: process integration, modelling and optimization for energy saving and pollution reduction. Asia-Pac J Chem Eng 2010;6:696–712.
[20] Calise F, Palombo A, Vanoli L. Design and dynamic simulation of a novel polygeneration system fed by vegetable oil and by solar energy. Energy Convers Manage 2012;60:204–13.
[21] Cheng ZD, He YL, Cui FQ, Xu RJ, Tao YB. Numerical simulation of a parabolic trough solar collector with nonuniform solar flux conditions by coupling FVM and MCRT method. Sol Energy 2012;86:1770–84.
[22] de Arce R, Mahia R, Medina E, Escribano G. A simulation of the economic impact of renewable energy development in Morocco. Energy Policy 2012;46:335–45.
[23] Xu E, Wang Z, Wei G, Zhuang J. Dynamic simulation of thermal energy storage system of Badaling 1 MW solar power tower plant. Renew Energy 2012;39:455–62.
[24] Xu R, Wiesner TF. Dynamic model of a solar thermochemical water-splitting reactor with integrated energy collection and storage. Int J Hydrogen Energy 2012;37:2210–23.
[25] Powell KM, Edgar TF. Modeling and control of a solar thermal power plant with thermal energy storage. Chem Eng Sci 2012;71:138–45.
[26] Manenti F. Natural gas operations: considerations on process transients, design, and control. ISA Trans 2012;51:317–24.
[27] Vitte P, Manenti F, Pierucci S, Joulia X, Buzzi-Ferraris G. Dynamic simulation of concentrating solar plants. Chem Eng Trans 2012:235–40.
[28] Bibler CJ, Marshall JS, Pilcher RC. Status of worldwide coal mine methane emissions and use. Int J Coal Geol 1998;35:283–310.
[29] Tewalt SJ, Willett JC, Finkelman RB. The world coal quality inventory: a status report. Int J Coal Geol 2005;63:190–4.
[30] Mohanty S, Nandha M, Habis E, Juhabi E. Oil price risk exposure: the case of the U.S. travel and leisure industry. Energy Econ 2014;41:117–24.
[31] Alquist R, Kilian L, Vigfusson RJ. Forecasting the price of oil. In: Elliott G, Timmermann A, editors. Handbook of economic forecasting, vol. 2. North-Holland: Amsterdam; 2013. p. 427–507 [chapter 8].
[32] Zhu HM, Li R. Modelling dynamic dependence between crude oil prices and Asia-Pacific stock market returns. Int Rev Econ Financ 2014;29:208–23.
[33] Perez JF, Meglar A, Benjumea PN. Effect of operating and design parameter on the gasification/combustion process of waste biomass in fixed bed downdraft reactors: an experimental study. Fuel 2012;96:487–96.
[34] Kumabe K, Hanaoaka T, Fujimoto S, Minowa T, Sakanishi K. Co-gasification of woody biomass and coal with air and steam. Fuel 2007;86:684–9.
[35] Ranzi E, Pierucci S, Aliprandi PC, Stringa S. Comprehensive and detailed kinetic model of a traveling grate combustor of biomass. Energy Fuels 2011;25:4195–205.
[36] Ranzi E, Corbetta M, Manenti F, Pierucci S. Kinetic modeling of the thermal degradation and combustion of biomass. Chem Eng Sci 2013.
[37] Bhavanam A, Sastry RS. Biomass gasification processes in downdraft fixed bed reactors: a review. Chem Eng Appl 2011;2:6.
[38] Basu P. Biomass gasification and pyrolysis. Elsevier; 2010. ISBN: 978-0-12-374988-8.
[39] Luo S, Guo X, Hu Z, Liu S, He M. Hydrogen-rich gas from catalytic steam gasification of biomass in a fixed bed reactor: influence of particle size on gasification particle. Hydrogen Energy 2009;34:1260–4.
[40] Lv PM, Xiong ZH, Chang J, Wu CZ, Chen Y, Zhu JX. An experimental study on biomass air-steam gasification in a fluidized bed. Biosource Technol 2004;95:95–101.
[41] Miguel GS, Dominguez MP, Hernandez M, Sanz-Perez F. Characterization and potential application of solid particles produced at a biomass gasification plant. Biomass Bioenergy 2012;47:134–44.
[42] Pedroso DT, Machin EB, Silveria JL, Nemoto Y. Experimental study of bottom feed updraft gasifier. Renew Energy 2013;57:311–6.
[43] Robinson PJ, Luyben WL. Integrated gasification combined cycle dynamic model: H_2S absorption/stripping, water gas shift reactors, and CO_2 absorption/stripping. Ind Eng Chem Res 2010;49:4766–81.
[44] Olah GA, Goeppert A, Surya Prakash GK. Beyond oil and gas: the methanol economy. Weinheim, Germany: Wiley-VCH; 2009.
[45] Gadek M, Kubica R, Jedrusik E. Production of methanol and dimethyl ether from biomass derived syngas – a comparison of the different synthesis pathways by means of flowsheet simulation. Comput Chem Eng 2013;32:55–60.
[46] Peduzzi E, Tock L, Boissonnet G, Maréchal F. Thermo-economic evaluation and optimization of the thermo-chemical conversion of biomass into methanol. Energy 2013;58:9–16.
[47] Holmgren KM, Berntsson T, Andersson E, Rydberg T. System aspects of biomass gasification with methanol synthesis – process concepts and energy analysis. Energy 2012;45:817–28.
[48] Kamarudin SK, Shamsul NS, Ghani JA, Chia SK, Liew HS, Samsudin AS. Production of methanol from biomass waste via pyrolysis. Bioresour Technol 2013;29:463–8.
[49] Manenti F, Adani F. Integrating the concept of bio-refinery onto the biogas field: the biorefill strategy. Comput Chem Eng 2014:1513–8. Elsevier.
[50] Lange JP. Methanol synthesis: a short review of technology improvements. Catal Today 2001;64:3–8.
[51] Shahrokhi M, Baghmisheh GR. Modeling, simulation and control of a methanol synthesis fixed-bed reactor. Chem Eng Sci 2005;60:4275–86.
[52] Manenti F, Cieri S, Restelli M, Bozzano G. Dynamic modelling of the methanol synthesis fixed-bed reactor. Comput Chem Eng 2013;48:325–34.

[53] Rahimpour MR. A dual-catalyst bed concept for industrial methanol synthesis. Chem Eng Commun 2007:194.
[54] Rahimpour MR. A two-stage catalyst bed concept for conversion of carbon dioxide into methanol. Fuel Process Technol 2008;89:556.
[55] Rahimpour MR, Pourzadi E, Iranshahi D, Bahmanpour AM. Methanol synthesis in a novel axial-flow, spherical packed bed reactor in the presence of catalyst deactivation. Chem Eng Res Des 2011;89:2457.
[56] Velardi SA, Barresi AA. Methanol synthesis in a forced unsteady-state reactor network. Chem Eng Sci 2002;57:2995–3004.
[57] Simsci-Esscor. PRO/II. User guide, Lake Forest, CA, USA; 2002. <www.simsci-esscor.com>.
[58] Simsci-Esscor. Dynamic simulation suite, user guide, Lake Forest, CA, USA; 2004. <www.simsci-esscor.com>.
[59] Buzzi-Ferraris G, Manenti F. BzzMath: library overview and recent advances in numerical methods. Comput Chem Eng 2012;30:1312–6.
[60] Buzzi-Ferraris G, Manenti F. Nonlinear systems and optimization for the chemical engineer: solving numerical problems. Weinheim, Germany: Wiley-VCH; 2014.
[61] Buzzi-Ferraris G, Manenti F. A combination of parallel computing and object-oriented programming to improve optimizer robustness and efficiency. Comput Chem Eng 2010;28:337–42.
[62] Manenti F, Buzzi-Ferraris G, Pierucci S, Rovaglio M, Gulati H. Process dynamic optimization using ROMeo. Comput Chem Eng 2011;29:452–6.
[63] HTRI; 2015. <https://www.htri.net/>.
[64] Ravaghi-Ardebili Z, Manenti F, Corbetta M, Pirola C, Ranzi E. Biomass gasification using low-temperature solar-driven steam supply. Renew Energy 2015;74:671–80.
[65] Winter DF. Solar collectors, energy storage, and materials. Massachusetts: The MIT Press; 1991.
[66] Tian Y, Zhao CY. A review of solar collectors and thermal energy storage in solar thermal. Appl Energy 2013;538:53.
[67] Ravaghi-Ardebili Z, Manenti F, Lima NMN, Linan LZ. Study of direct thermal energy storage technologies for effectiveness of concentrating solar power plants. Chem Eng Trans 2013;32:1219–24.
[68] Gil A, Medrano M, Martorell I. State of the art on high temperature thermal energy storage for power generation, Part 1-concepts, materials and modellization. Renew Sustain Energy Rev 2010;14:31–55.
[69] Herrmann H, Kelly B. Two-tank molten salt storage for parabolic trough solar. Price Energy 2004;29:883–93.
[70] Oro E, Gil A, Gracia A. Comparative life cycle assessment of thermal energy storage systems for solar power plants. Renew Energy 2012;44: 166–73.
[71] Manenti G. A calculation procedure for a heat exchanger and bypass equipment. Comput Chem Eng 2011;35:2378–88.
[72] Taborek J. Performance of shell-and-tube heat exchanger with double-segmental baffles. College Station, TX: Heat Transfer Research Inc.; 1972.
[73] Churchill H, Chu HS. Correlating equations for laminar and turbulent free convection from a horizontal cylinder. Int J Heat Mass Transf 1975.
[74] Flueckiger S, Yang Z, Garimella SV. An integrated thermal and mechanical investigation of molten salt thermocline energy storage. Appl Energy 2011;88:2098–105.
[75] Badeau JP, Levi A. Biomass gasification: chemistry, process and application. Nova Science Publisher; 2009. ISBN: 978-1-61122-683-6.
[76] Hertwich EG, Zhang X. Concentrating-solar biomass gasification process for a 3rd generation biofuel. Environ Sci Technol 2009;43:4707–12.
[77] Ranz WE, Marshall WR. Evaporation from drops, Part I. Chem Eng Prog 1952;48:141–6.
[78] Ravaghi-Ardebili Z, Manenti F. Direct solar-powered biomass gasification using low-temperature steam. AICHE annual meeting, San Francisco; 2013.
[79] Faravelli T, Frassoldati A, Migliavacca G, Ranzi E. Detailed kinetic modeling of the thermal degradation of lignins. Biomass Bioenergy 2010;34:290–301.
[80] Kumar A, Eskridge K, Jones DD, Hanna MA. Steam–air fluidized bed gasification of distillers grains: effects of steam to biomass ratio, equivalence ratio and gasification temperature. Bioresour Technol 2009;100:2062–8.
[81] Sandeep K, Dasappa S. Oxy-Steam gasification of biomass for hydrogen rich syngas production using downdraft reactor configuration. Int J Energy 2013.
[82] Timmerhause KD. Plant design and economics for chemical engineering. McGraw-Hill; 1991. ISBN: 0070496137.
[83] Diaz MS, Espoinosa S, Brignole EA. Model-based cost minimization in noncatalytic biodiesels production plant. Energy Fuels 2009;23:5587–95.
[84] Sinnott RK. Chemical engineering design. Coulson & Richardson's chemical engineering series; 2005. ISBN-13: 978-0750665384.
[85] Manenti F, Cieri S, Restelli M. Considerations on the steady-state modeling of methanol synthesis fixed-bed reactor. Chem Eng Sci 2011;66:152–62.
[86] Manenti F, Bozzano G. Optimal control of methanol synthesis fixed-bed reactor. Ind Eng Chem Res 2013;52:13079–91.
[87] Manenti F, Cieri S, Restelli M, Bozzano G. Dynamic modeling of the methanol synthesis fixed-bed reactor. Comput Chem Eng 2013;48:325–34.
[88] Larson ED, Tingjin R. Synthetic fuel production by indirect coal liquefaction. Energy Sustain Dev 2003;7:79–102.
[89] Ravaghi-Ardebili Z, Manenti F, Lima NNN, Linan LZ, Cieri S, Restelli M, et al. Preserving safety and improving yield performances in methanol processes. Chem Eng Trans 2012;26:69–74.
[90] Ju F, Chen H, Ding X, Yang H, Wang X, Zhang S, et al. Process simulation of single-step dimethyl ether production via biomass gasification. Biotechnol Adv 2009;27:599–605.
[91] Manenti F, Cieri S, Restelli M, Lima NMN, Lamia ZL. Dynamic simulation of the lurgi-type reactor for methanol synthesis. Chem Eng Trans 2011;24:379–84.
[92] Manenti F, Cieri S, Restelli M, Lima NMN, Zuniga Linan L, Bozzano G. Online feasibility and effectiveness of a spatio-temporal nonlinear model predictive control. The case of methanol synthesis reactor. Comput Chem Eng 2012;30:867–71.
[93] Lommerts BJ, Graaf GH, Beenackers A. Mathematical modeling of internal mass transport limitations in methanol synthesis. Chem Eng Sci 2000;55:5589–98.
[94] Graaf GH, Sijtsema PJ, Stamhuis EJ, Joosten GE. Chemical equilibria in methanol synthesis. Chem Eng Sci 1986;41:2883–90.
[95] Graaf GH, Stamhuis EJ, Beenackers A. Kinetics of low-pressure methanol synthesis. Chem Eng Sci 1988;43:3185–95.
[96] Bercic G, Levec J. Intrinsic and global reaction rate of methanol dehydration over. gamma.-alumina pellets. Ind Eng Chem Res 1992;31:1035.
[97] Rachford HH, Rice JD. Procedure for use of electrical digital computers in calculating flash vaporization hydrocarbon equilibrium. Trans AIME 1952;4:195.
[98] Manenti F, Leon-Garzon AR, Ravaghi-Ardebili Z, Pirola C. Systematic staging design applied to the fixed-bed reactor series for methanol and one-step methanol/dimethyl ether synthesis. Appl Therm Eng 2014.